ENGINEERING Information Technology & Electronic Engineering
https://www.academax.com/EITEE; https://www.engineering.org.cn
https://ieeexplore.ieee.org/xpl/RecentIssue.jsp?punumber=11344065
E-mail: eng.itee@zju.edu.cn

Engineering Journals
Available on IEEE Xplore

Research Article
https://doi.org/10.1631/ENG.ITEE.2026.0090

Continuous aperture array-assisted integrated communication and navigation in low Earth orbit satellite constellations

Qi WANG[1], Xiaoming CHEN[1✉], Qiao QI[2], Zhaolin WANG[3], Yuanwei LIU[3]

[1]*College of Information Science and Electronic Engineering, Zhejiang University, Hangzhou 310027, China*
[2]*School of Information Science and Technology, Hangzhou Normal University, Hangzhou 311121, China*
[3]*Department of Electrical and Computer Engineering, The University of Hong Kong, Hong Kong 999077, China*

Abstract: This paper proposes a novel continuous aperture array (CAPA)-assisted integrated communication and navigation (ICAN) framework for low Earth orbit (LEO) satellite constellations. Within this framework, an electromagnetic-based collaborative transmission model is developed, in which multiple satellites equipped with CAPAs simultaneously radiate downlink data streams and navigation reference signals over a shared spectrum. Building upon this, the achievable communication rate and the navigation Cramér–Rao bound (CRB) are derived, which explicitly characterize the intrinsic coupling between the dual-function beamformers and system performance. To improve the positioning accuracy with a communication quality of service guarantee, a joint beamforming optimization problem is formulated to minimize the average CRB subject to transmit power budgets and minimum rate constraints. To tackle the inherent infinite dimensionality of the CAPA beamformer design, an ICAN channel subspace is introduced to equivalently transform the formulation into a tractable finite-dimensional problem, which is then efficiently solved via an iterative convex optimization algorithm. Finally, numerical results demonstrate that the proposed CAPA-assisted beamforming design algorithm significantly outperforms conventional discrete phased array architectures and other benchmark schemes, yielding notable improvements in ICAN performance.

Key words: Sixth-generation (6G); Electromagnetic information theory; Low Earth orbit (LEO) satellite constellation; Continuous aperture array; Integrated communication and navigation (ICAN)

1 Introduction

The advent of the sixth-generation (6G) mobile communication era is accelerating the evolution of wireless networks toward global connectivity, where low Earth orbit (LEO) satellite constellations, as an important component of non-terrestrial networks (NTNs), are expected to play a key role (Jin et al., 2022). By deploying thousands of satellites worldwide, these mega-constellations aim to provide space-based connectivity with seamless coverage, low latency, and high throughput (Ying et al., 2026).

Beyond communication, dense LEO satellite constellations also offer an attractive platform for high-performance positioning, navigation, and timing (PNT) services. Compared with the traditional global navigation satellite system (GNSS) operating in medium and high orbits, LEO satellite constellations can provide improved geometry and signal conditions due to their orbital characteristics and enhanced visibility, which enables stronger geometric diversity and a more robust signal environment (Iannucci and Humphreys, 2024). These features have motivated integrated communication and navigation (ICAN) as an emerging direction for 6G networks (You et al., 2024; Liu JY et al., 2025). By jointly designing communication and navigation functions on a shared platform, ICAN can improve spectrum and hardware utilization, reduce deployment cost and payload complexity, and deliver performance gains for both services.

However, achieving high-performance ICAN is constrained by conventional antenna technologies, particularly spatially discrete phased arrays (DPAs) that are

✉ Xiaoming CHEN, chen_xiaoming@zju.edu.cn
Qi WANG, https://orcid.org/0000-0002-8079-2161
Xiaoming CHEN, https://orcid.org/0000-0002-1818-2135
Qiao QI, https://orcid.org/0000-0002-5120-6186
Zhaolin WANG, https://orcid.org/0000-0003-4614-0175
Yuanwei LIU, https://orcid.org/0000-0002-6389-8941
CLC number: TN927.2

Received: Apr. 1, 2026; Revision accepted: June 16, 2026; Crosschecked: June 24, 2026; Published online: July 23, 2026

Academic Paper of the 28th Annual Meeting of the China Association for Science and Technology

© The Authors 2026. Published by Zhejiang University Press Co., Ltd. This is an open access article distributed under the terms of the CC BY-NC-ND license (https://creativecommons.org/licenses/by-nc-nd/4.0/)

widely used in current satellite payloads. The high orbital velocity of LEO satellites requires agile and continuous beam tracking. In practice, discrete arrays suffer from scan-angle-dependent gain loss, quantization errors, and non-negligible calibration overhead, which makes it difficult to meet these requirements (Feng and Jenn, 2015). To alleviate these limitations, holographic multiple-input multiple-output (MIMO) and dynamic metasurface architectures have been explored by using densely packed elements to approximate a continuous aperture (Wang HQ et al., 2021; Jin et al., 2024). In particular, the performance analysis and holographic beamforming methods for holographic MIMO communications have been systematically reviewed in An et al. (2023). More recently, stacked intelligent metasurfaces (SIMs) have also been investigated for LEO satellite communications, where statistical channel state information (CSI) is exploited to support wave-domain beamforming and reduce the dependence on instantaneous CSI acquisition (Lin et al., 2024). Nevertheless, these holographic, metasurface, and SIM-based architectures are still implemented through discretized or layer-wise controllable elements, and typically cannot realize a truly continuous current distribution. As discussed in Wang Z et al. (2025), this prevents them from fully exploiting the electromagnetic degrees of freedom offered by the aperture. Moreover, ICAN imposes concurrent beamforming requirements, including highly directional multiuser beams for communication and broad and structured radiation patterns for navigation, which further increases the implementation complexity and power consumption of discrete architectures.

To address these limitations, a continuous aperture array (CAPA) architecture is introduced as an appealing solution. CAPA is rooted in electromagnetic information theory, which studies the fundamental limits of wireless systems by directly modeling radiating surfaces and wave propagation (Jensen and Wallace, 2008). Unlike DPAs, a CAPA is modeled as a continuous radiating surface that supports a spatially continuous current distribution over the aperture, thereby providing additional degrees of freedom for electromagnetic field synthesis. Ouyang et al. (2024) demonstrated that CAPAs can achieve high spatial degrees of freedom, and Liu YW et al. (2025) investigated the corresponding channel capacity, showing notable gains over discrete arrays of comparable size. Building on these foundations, Wang ZL et al. (2025b) developed a CAPA beamforming framework for multiuser downlink transmission, further illustrating the design flexibility enabled by continuous apertures. Collectively, these research findings suggest that CAPA is a promising enabler for ICAN, as it can support high-gain directional transmission for communication and can potentially accommodate the wide-coverage and structured radiation required for navigation.

Despite this potential, several challenges remain in designing CAPA-assisted ICAN systems. While recent efforts have started to explore beamforming for CAPA-enabled dual-functional transmission, most existing studies consider a single CAPA radiator deployed on a single platform. For instance, Zhao BQ et al. (2026) investigated downlink and uplink integrated sensing and communication (ISAC) transmission in CAPA systems and developed corresponding beamforming designs for dual-functional operation. Zhang Y et al. (2026) studied CAPA-enabled ISAC from a rate-Cramér–Rao bound (rate-CRB) perspective and proposed a beamforming framework to characterize and optimize the inherent sensing-communication trade-off. In addition to this system-level limitation, existing works also face a methodological challenge in solving continuous-aperture beamforming problems. A common approach is to discretize the continuous-aperture beamforming problem via Fourier series expansions. For example, Sanguinetti et al. (2023) approximated the continuous source current distribution using a finite set of Fourier basis functions, which turns the original functional optimization into a high-dimensional finite-dimensional problem, and the required basis size can grow rapidly with the aperture size and carrier frequency. To avoid such discretization-induced accuracy-complexity issues, Wang ZL et al. (2026) developed a calculus-of-variations-based design, where closed-form updates are derived within an iterative weighted minimum mean-squared error (WMMSE) framework to directly optimize the continuous beamformers without relying on discretization approximations. However, for NTN scenarios such as LEO satellite constellations, these single-platform formulations do not readily extend to cooperative multi-satellite transmission with multiple CAPAs where satellite propagation channels differ fundamentally from terrestrial channels. Consequently, how to systematically exploit multiple CAPAs in an LEO satellite constellation for ICAN, while balancing communication throughput and navigation accuracy, remains largely unexplored.

Motivated by the aforementioned research gaps, this paper develops a CAPA-assisted ICAN framework for LEO satellite constellations, and proposes a tractable subspace-based approach for joint beamforming design. The main contributions are summarized as follows:

1. We propose a CAPA-assisted ICAN architecture for LEO satellite constellations with cooperative multi-satellite transmission, and establish an electromagnetic-based continuous-aperture model to derive the achievable rates of communication user equipment (CUE) and the CRBs of navigation user equipment (NUE).

2. We formulate a joint beamforming design problem that minimizes the average CRB of NUE subject to per-satellite transmit power budgets and minimum achievable rate constraints for all CUE, thereby characterizing the fundamental accuracy–throughput trade-off in ICAN.

3. We introduce an ICAN channel subspace to transform the infinite-dimensional CAPA beamforming design into an equivalent finite-dimensional formulation, based on which we develop an efficient iterative convex optimization algorithm to obtain feasible solutions.

Notations: Scalars, vectors, and matrices are denoted by regular letters, boldface lowercase letters, and boldface uppercase letters, respectively. For complex-valued quantities, $(\cdot)^*$, $(\cdot)^{\mathrm{T}}$, and $(\cdot)^{\mathrm{H}}$ represent the complex conjugate, transpose, and conjugate transpose, respectively, and $\Re\{\cdot\}$ extracts the real part. The matrix inverse is denoted by $(\cdot)^{-1}$. The Euclidean norm of a vector is written as $\|\cdot\|$, and $\times$ denotes the cross product of two three-dimensional vectors. For a matrix, $\mathrm{tr}(\cdot)$ and $\mathrm{rank}(\cdot)$ denote the trace and rank, respectively. The block-diagonal operator is denoted by $\mathrm{blkdiag}(\cdot)$, and $\boldsymbol{X} \succeq 0$ indicates that $\boldsymbol{X}$ is positive semidefinite. The sets of complex- and real-valued $(a \times b)$-dimensional matrices are denoted by $\mathbb{C}^{a\times b}$ and $\mathbb{R}^{a\times b}$, respectively. The asymptotic computational complexity is expressed using the notation $O(\cdot)$.

2 System model

Consider an LEO satellite constellation-based ICAN system, as shown in Fig. 1. The constellation follows a Walker Delta configuration, comprising a large number of LEO satellites arrayed in multiple equally inclined circular orbital planes with evenly spaced right ascension of the ascending node (RAAN) and uniform in-plane phasing. Each satellite is equipped with a geocentric nadir-pointing CAPA transmitter that radiates electromagnetic waves supporting both data communication and position navigation over a shared spectrum, realized via a continuous and precisely controllable sinusoidal source current distribution across its radiating surface. Without loss of generality, at any given time, a subset of K satellites is dynamically selected as a collaborative service group to jointly serve M single-antenna CUEs and L single-antenna NUEs within their terrestrial coverage area. Enabled by high-speed, low-latency inter-satellite links (ISLs), the satellites in the service group exchange CSI and ephemeris data in real time, enabling coordinated multi-satellite joint transmission. Through satellite–terrestrial links, CUE decodes modulated data streams for global connectivity, whereas NUE exploits dedicated navigation reference signals to achieve high-precision positioning.

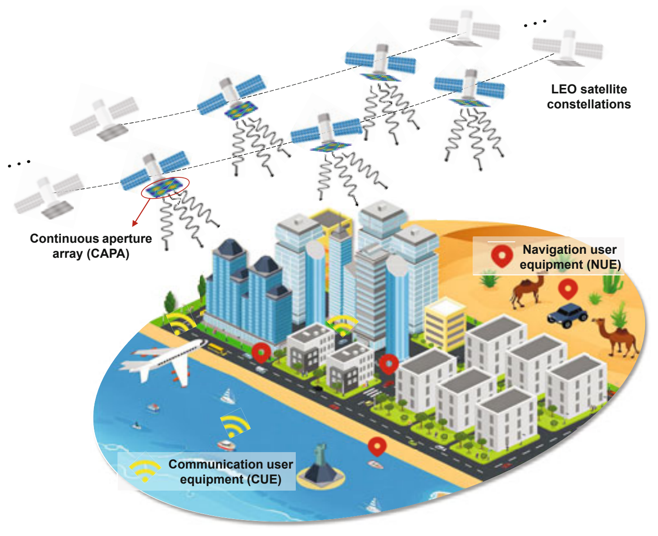

Fig. 1 System model for CAPA-assisted ICAN in LEO satellite constellation

To enable a rigorous mathematical description, we first establish the coordinate frames. Here, the Earth-centered, Earth-fixed (ECEF) frame is adopted as the global Cartesian reference, with its origin at the Earth's center of mass, the x-axis pointing toward the intersection of the equator and the Greenwich meridian, the y-axis pointing eastward along the equator, and the z-axis aligned with the rotation axis toward the North Pole. In this context, the positions of the k^{th} satellite, the m^{th} CUE, and the l^{th} NUE can be denoted by vectors $\boldsymbol{r}_k = [r_k^x, r_k^y, r_k^z]^{\mathrm T}$, $\boldsymbol{p}_m = [p_m^x, p_m^y, p_m^z]^{\mathrm T}$, and $\boldsymbol{q}_l = [q_l^x, q_l^y, q_l^z]^{\mathrm T}$, respectively, all expressed in the ECEF frame. In parallel, for each satellite, a local orbital frame (LOF) is defined with its origin at the CAPA surface center, x'-axis forming a right-handed triad, y'-axis along the instantaneous velocity, and z'-axis pointing toward Earth's center. The transformation from the LOF to the global ECEF frame can be realized by a rotation matrix $\boldsymbol{R}_k \in \mathbb{R}^{3\times 3}$, which is uniquely determined by the satellite's ECEF position $\boldsymbol{r}_k$ and velocity $\boldsymbol{v}_k$. In this context, the CAPA on the k^{th} satellite is modeled as a rectangular surface $\boldsymbol{S}_k'$ lying in the x'–y' plane of its LOF:

$$\boldsymbol{S}_k' = \left\{ \boldsymbol{s}_k' = (s_k'^{\,x}, s_k'^{\,y}, 0)^{\mathrm T} \;\middle|\; |s_k'^{\,x}| \le \frac{D_x}{2},\ |s_k'^{\,y}| \le \frac{D_y}{2} \right\}, \tag{1}$$

where D_x and D_y are the aperture side lengths, and $|\boldsymbol{S}_k'| = D_x D_y = A_{\mathrm T}$, with $A_{\mathrm T}$ denoting the effective radiating area of the CAPA. Herein, $\boldsymbol{s}_k' \in \boldsymbol{S}_k'$ denotes the LOF coordinates of an arbitrary point on the CAPA of the k^{th} satellite. Accordingly, the ECEF position $\boldsymbol{s}_k$ of any point on this surface is obtained by mapping its LOF coordinate $\boldsymbol{s}_k'$ with the satellite's pose and is given by

$$\boldsymbol{s}_k = \boldsymbol{r}_k + \boldsymbol{R}_k \boldsymbol{s}_k'. \tag{2}$$

This geometric formulation provides a precise description of the spatial location and attitude of the k^{th} satellite's CAPA, forming the basis for the transmit, propagation, communication, and navigation models.

2.1 Transmit model

To simultaneously serve multiple CUEs for downlink communications and multiple NUEs for terrestrial navigation, the k^{th} satellite transmits a superposition of M downlink data streams and one dedicated navigation reference signal. Let $x_m^{\mathrm C}$ denote the complex data symbol intended for the m^{th} CUE, which is modeled as an independent, zero-mean circularly symmetric complex Gaussian random variable with normalized power, i.e., $\mathbb{E}\big[|x_m^{\mathrm C}|^2\big] = 1$. Likewise, let $x_k^{\mathrm N}$ represent the navigation reference signal emitted by the k^{th} satellite, modeled as a deterministic unit-power pseudo-random sequence, i.e., $\langle |x_k^{\mathrm N}|^2 \rangle_T = 1$, and time-balanced such that $\langle x_k^{\mathrm N} \rangle_T = 0$, where $\langle \cdot \rangle_T \triangleq \frac{1}{T}\int_0^T (\cdot)\,\mathrm{d}t$ denotes time averaging over a sufficiently long interval T. The known pseudo-random waveform $x_k^{\mathrm N}$ serves as a receiver-side spreading code reference to extract position and Doppler-dependent features via matched filtering. Moreover, the random data symbols $x_m^{\mathrm C}$ and the deterministic navigation signals $x_k^{\mathrm N}$ are assumed to be mutually uncorrelated. To radiate these scalar signals into physical space via a CAPA, a mapping from the signal domain to the continuous aperture domain is required.

Unlike conventional discrete arrays that apply complex weights to a finite set of antenna elements, a CAPA enables continuous spatial modulation of the surface current across the aperture. Accordingly, we characterize the CAPA excitation corresponding to the above superposed baseband signals by a surface current density distribution over the continuous aperture. Specifically, let $\tilde{\boldsymbol{J}}(\boldsymbol{s}_k, \varpi) \in \mathbb{C}^{3\times 1}$ denote the Fourier transform of the source current density at an ECEF coordinate $\boldsymbol{s}_k$, where $\varpi = 2\pi f / c$ is the spatial angular frequency, with f being the carrier frequency and c being the speed of light. Since all satellites operate on the same carrier frequency

f, we omit the explicit dependence on ϖ and write $\tilde{\boldsymbol{J}}(\boldsymbol{s}_k)$ for brevity. Because the CAPA is mounted on the satellite platform, the current distribution is most naturally specified in the LOF. We focus on a uni-polarized CAPA, where the current is excited exclusively along the LOF y'-axis, represented by $\hat{\boldsymbol{u}}'_y = [0,1,0]^{\mathrm{T}}$. The corresponding polarization direction in the ECEF frame is $\hat{\boldsymbol{u}}_{k,y} = \boldsymbol{R}_k \hat{\boldsymbol{u}}'_y$. Under this setting, the source current vector in ECEF can be expressed as

$$\tilde{\boldsymbol{J}}(\boldsymbol{s}_k) = j(\boldsymbol{s}'_k)\,\hat{\boldsymbol{u}}_{k,y}, \tag{3}$$

where $j(\boldsymbol{s}'_k)$ (in ampere per meter, A/m) is the scalar surface current field that captures the complex amplitude–phase distribution over the continuous CAPA aperture $\boldsymbol{S}'_k$ in LOF coordinates.

Leveraging the linearity of electromagnetic radiation with respect to the source, we model the scalar current field as a linear superposition of communication and navigation-bearing components, which is given by

$$j(\boldsymbol{s}'_k) = \sum_{m=1}^{M} w_{k,m}(\boldsymbol{s}'_k)\, x_m^{\mathrm{C}} + v_k(\boldsymbol{s}'_k)\, x_k^{\mathrm{N}}. \tag{4}$$

Herein, $w_{k,m}(\boldsymbol{s}'_k)$ is the continuous transmit beamformer representing the source current pattern at $\boldsymbol{s}'_k$ tailored for the m^{th} CUE, and $v_k(\boldsymbol{s}'_k)$ is the continuous transmit beamformer designed for navigation services.

Based on these properties, the total average transmit power at the k^{th} satellite is derived by taking both the statistical and time averages of the instantaneous power, which is expressed as

$$\begin{aligned} P_k &= \mathbb{E}\left[\left\langle \int_{\boldsymbol{S}'_k} \left|j(\boldsymbol{s}'_k)\right|^2 \mathrm{d}\boldsymbol{s}'_k \right\rangle_T\right] \\ &\overset{\text{(a)}}{=} \int_{\boldsymbol{S}'_k} \left(\sum_{m=1}^{M} |w_{k,m}(\boldsymbol{s}'_k)|^2 \mathbb{E}[|x_m^{\mathrm{C}}|^2] + |v_k(\boldsymbol{s}'_k)|^2 \langle |x_k^{\mathrm{N}}|^2 \rangle_T \right) \mathrm{d}\boldsymbol{s}'_k \\ &\overset{\text{(b)}}{=} \sum_{m=1}^{M} \int_{\boldsymbol{S}'_k} |w_{k,m}(\boldsymbol{s}'_k)|^2 \mathrm{d}\boldsymbol{s}'_k + \int_{\boldsymbol{S}'_k} |v_k(\boldsymbol{s}'_k)|^2 \mathrm{d}\boldsymbol{s}'_k. \end{aligned} \tag{5}$$

The equality in (a) follows from the uncorrelated nature of all distinct signal components, which makes the cross terms average to zero. The equality in (b) follows directly from the unit power normalization of both communication and navigation signals.

2.2 Propagation model

The electromagnetic field radiated by the source current $\boldsymbol{J}(\boldsymbol{s}_k)$ on the CAPA surface propagates through the atmosphere in a homogeneous medium to the ground users. According to Maxwell's equations, the total electric field $\boldsymbol{E}_m^{\mathrm{C}}$ at location $\boldsymbol{p}_m$ of the m^{th} CUE, due to the K cooperating satellites, is given by the superposition of surface integrals over each satellite's aperture (Dardari, 2020):

$$\boldsymbol{E}_m^{\mathrm{C}} = \sum_{k=1}^{K} \int_{\boldsymbol{S}'_k} \boldsymbol{G}_{k,m}^{\mathrm{C}}\left(\boldsymbol{s}_k(\boldsymbol{s}'_k), \boldsymbol{p}_m\right) \tilde{\boldsymbol{J}}(\boldsymbol{s}_k(\boldsymbol{s}'_k))\mathrm{d}\boldsymbol{s}'_k. \tag{6}$$

Similarly, the electric field $\boldsymbol{E}_l^{\mathrm{N}}$ experienced by the l^{th} NUE at location $\boldsymbol{q}_l$ is expressed as

$$\boldsymbol{E}_l^{\mathrm{N}} = \sum_{k=1}^{K} \int_{\boldsymbol{S}'_k} \boldsymbol{G}_{k,l}^{\mathrm{N}}\left(\boldsymbol{s}_k(\boldsymbol{s}'_k), \boldsymbol{q}_l\right) \tilde{\boldsymbol{J}}(\boldsymbol{s}_k(\boldsymbol{s}'_k))\mathrm{d}\boldsymbol{s}'_k. \tag{7}$$

Note that the integration is carried out over the local coordinate $\boldsymbol{s}'_k$ on the surface $\boldsymbol{S}'_k$, whereas the integrand is evaluated at the corresponding global ECEF position $\boldsymbol{s}_k(\boldsymbol{s}'_k)$. Furthermore, the integral kernels $\boldsymbol{G}_{k,m}^{\mathrm{C}}(\cdot)$ and $\boldsymbol{G}_{k,l}^{\mathrm{N}}(\cdot)$ are dyadic Green's functions for line-of-sight (LoS) propagation. In the far-field region, where the electromagnetic field has attained its radiating form, $\boldsymbol{G}_{k,m}^{\mathrm{C}}(\cdot)$ is well-approximated by Wang ZL et al. (2025a):

$$\begin{aligned} \boldsymbol{G}_{k,m}^{\mathrm{C}}\left(\boldsymbol{s}_k, \boldsymbol{p}_m\right) = &- \frac{\mathrm{j}\eta \mathrm{e}^{-\mathrm{j}\frac{2\pi}{\lambda}\|\boldsymbol{p}_m - \boldsymbol{s}_k\|}}{2\lambda\|\boldsymbol{p}_m - \boldsymbol{s}_k\|} \xi_{\mathrm{r}}^{\frac{1}{2}} \mathrm{e}^{-\mathrm{j}\psi_{k,m}} \mathrm{e}^{-\mathrm{j}\phi_{k,m}^{\mathrm{D}}} \\ &\cdot \left(\boldsymbol{I}_3 - \frac{(\boldsymbol{p}_m - \boldsymbol{s}_k)(\boldsymbol{p}_m - \boldsymbol{s}_k)^{\mathrm{T}}}{\|\boldsymbol{p}_m - \boldsymbol{s}_k\|^2} \right), \end{aligned} \tag{8}$$

where $\eta = 120\pi\ \Omega$ is the intrinsic impedance of free space, λ denotes the signal wavelength, and $\boldsymbol{I}_3$ is the 3×3 identity matrix. Moreover, rain attenuation is captured by the amplitude–phase pair $(\xi_{\mathrm{r}}^{1/2}, \psi_{k,m})$, with the amplitude factor ξ_{r} modeled as log-normal so that $\ln(\xi_{\mathrm{r}}^{1/2}) \sim \mathcal{N}(\mu_{\mathrm{r}}, \sigma_{\mathrm{r}}^2)$ and $\psi_{k,m}$ denotes the associated rain-induced phase perturbation (Ying et al., 2024). The term $\mathrm{e}^{-\mathrm{j}\phi_{k,m}^{\mathrm{D}}}$ denotes the Doppler shift caused by the LEO satellite motion, which can be estimated and compensated by standard receiver synchronization such as carrier tracking and is omitted in the subsequent analysis (Li et al., 2022). Green's function for the navigation link $\boldsymbol{G}_{k,l}^{\mathrm{N}}(\boldsymbol{s}_k, \boldsymbol{q}_l)$ has an identical mathematical structure.

To sense the full three-dimensional electric field, each CUE and NUE would require an ideal tri-polarized receiver, which is challenging to implement in practice. Accordingly, we assume that each user employs a uni-polarized antenna. This assumption models practical low-complexity CUE and NUE by projecting the vector electric field onto a fixed receive polarization direction. It neglects multi-polarization reception and polarization combining. In practical LEO satellite–ground links, attitude variations, terminal orientation errors, cross-polar leakage, and propagation-induced polarization changes may cause polarization mismatch, thereby affecting the received signal power, achievable rate, and CRB performance. For the m^{th} CUE, the receive polarization is described by a real unit vector $\boldsymbol{u}_m \in \mathbb{R}^{3\times 1}$ with $\|\boldsymbol{u}_m\| = 1$, so that only the field component along $\boldsymbol{u}_m$ is observed. Without loss of generality, all CUE antennas are assumed to be y-directed linearly polarized in ECEF, i.e., $\boldsymbol{u}_m = [0,1,0]^{\mathrm{T}}$. To facilitate electromagnetic propagation analysis, we define an effective spatially continuous channel response $h_{k,m}^{\mathrm{C}}$ from an arbitrary point $\boldsymbol{s}'_k$ on the satellite's CAPA to the m^{th} CUE. This channel response accounts for the dyadic Green's function as well as transmit and receive polarization effects and is given by

$$h_{k,m}^{\mathrm{C}}\left(\boldsymbol{s}'_k, \boldsymbol{p}_m\right) = \boldsymbol{u}_m^{\mathrm{T}} \boldsymbol{G}_{k,m}^{\mathrm{C}}\left(\boldsymbol{s}_k(\boldsymbol{s}'_k), \boldsymbol{p}_m\right) \hat{\boldsymbol{u}}_{k,y}. \tag{9}$$

Similarly, the spatially continuous channel response $h_{k,l}^{\mathrm{N}}$ from the same radiating point to the l^{th} NUE is given by

$$h_{k,l}^{\mathrm{N}}\left(\boldsymbol{s}'_k, \boldsymbol{q}_l\right) = \boldsymbol{u}_l^{\mathrm{T}} \boldsymbol{G}_{k,l}^{\mathrm{N}}\left(\boldsymbol{s}_k(\boldsymbol{s}'_k), \boldsymbol{q}_l\right) \hat{\boldsymbol{u}}_{k,y}, \tag{10}$$

where $\boldsymbol{u}_l \in \mathbb{R}^{3\times 1}$ denotes the unit receive polarization vector of the l^{th} NUE, defined in the same manner as $\boldsymbol{u}_m$. These channel response functions provide a rigorous and concise foundation for formulating the system performance metrics for both communication and navigation, as detailed in the following subsections.

2.3 Communication model

With the effective channel responses established, we now formulate the signal reception model for the communication service. The total signal received by the m^{th} CUE is the coherent superposition of the electromagnetic waves radiated by the service group of K satellites, corrupted by additive thermal noise. By invoking the source current definition in Eq. (4) and the continuous channel response $h^{\text{C}}_{k,m}(\boldsymbol{s}'_k, \boldsymbol{p}_m)$ derived in Eq. (9), the received signal y^{C}_m at the m^{th} CUE can be expressed as

$$\begin{aligned} y^{\text{C}}_m &= \sum_{k=1}^{K} \int_{\boldsymbol{S}'_k} h^{\text{C}}_{k,m}(\boldsymbol{s}'_k, \boldsymbol{p}_m)\, j(\boldsymbol{s}'_k)\, \mathrm{d}\boldsymbol{s}'_k + n^{\text{C}}_m \\ &= \underbrace{\left(\sum_{k=1}^{K} \int_{\boldsymbol{S}'_k} h^{\text{C}}_{k,m}(\boldsymbol{s}'_k, \boldsymbol{p}_m)\, w_{k,m}(\boldsymbol{s}'_k)\, \mathrm{d}\boldsymbol{s}'_k\right) x^{\text{C}}_m}_{\text{Desired communication signal}} \\ &\quad + \underbrace{\sum_{i=1, i\neq m}^{M} \left(\sum_{k=1}^{K} \int_{\boldsymbol{S}'_k} h^{\text{C}}_{k,m}(\boldsymbol{s}'_k, \boldsymbol{p}_m)\, w_{k,i}(\boldsymbol{s}'_k)\, \mathrm{d}\boldsymbol{s}'_k\right) x^{\text{C}}_i}_{\text{Inter-CUE interference}} \\ &\quad + \underbrace{\sum_{k=1}^{K} \left(\int_{\boldsymbol{S}'_k} h^{\text{C}}_{k,m}(\boldsymbol{s}'_k, \boldsymbol{p}_m)\, v_k(\boldsymbol{s}'_k)\, \mathrm{d}\boldsymbol{s}'_k\right) x^{\text{N}}_k}_{\text{Navigation interference}} + \underbrace{n^{\text{C}}_m}_{\text{Noise}}. \end{aligned} \tag{11}$$

The first term of the right-hand side is the desired communication signal, namely, the coherent superposition of transmissions from all K cooperating satellites intended for the m^{th} CUE. The integral $\sum_{k=1}^{K} \int_{\boldsymbol{S}'_k} h^{\text{C}}_{k,m}(\cdot) w_{k,m}(\cdot) \mathrm{d}\boldsymbol{s}'_k$ acts as the effective cooperative channel gain from the service group to $\boldsymbol{p}_m$. The next two terms constitute the interference. Inter-CUE interference arises from energy radiated by the continuous transmit beamformers $w_{k,i}(\boldsymbol{s}'_k)$ designed for other CUE ($i \neq m$), which leaks toward the m^{th} CUE. Navigation interference is generated by the navigation continuous transmit beamformers $v_k(\boldsymbol{s}'_k)$, an intrinsic coupling of the ICAN architecture. The last term n^{C}_m denotes the thermal noise at the m^{th} CUE, modeled as independent additive white Gaussian noise (AWGN) with zero mean and variance $\sigma^2_{\text{C},m}$.

Based on the decomposition in Eq. (11) and the statistical independence of the transmitted symbols, the signal-to-interference-plus-noise ratio (SINR) received at the m^{th} CUE is given by

$$\gamma_m = \frac{\left|\sum_{k=1}^{K} \int_{\boldsymbol{S}'_k} h^{\text{C}}_{k,m}(\boldsymbol{s}'_k, \boldsymbol{p}_m) w_{k,m}(\boldsymbol{s}'_k) \mathrm{d}\boldsymbol{s}'_k\right|^2}{I_{m,\text{CUE}} + I_{m,\text{NAV}} + \sigma^2_{\text{C},m}}, \tag{12}$$

where the interference powers are defined as

$$I_{m,\text{CUE}} = \sum_{i=1, i\neq m}^{M} \left|\sum_{k=1}^{K} \int_{\boldsymbol{S}'_k} h^{\text{C}}_{k,m}(\boldsymbol{s}'_k, \boldsymbol{p}_m) w_{k,i}(\boldsymbol{s}'_k) \mathrm{d}\boldsymbol{s}'_k\right|^2, \tag{13}$$

$$I_{m,\text{NAV}} = \sum_{k=1}^{K} \left|\int_{\boldsymbol{S}'_k} h^{\text{C}}_{k,m}(\boldsymbol{s}'_k, \boldsymbol{p}_m) v_k(\boldsymbol{s}'_k) \mathrm{d}\boldsymbol{s}'_k\right|^2. \tag{14}$$

Finally, the achievable rate of the m^{th} CUE is determined by the Shannon–Hartley theorem, given by

$$R_m = \log_2(1 + \gamma_m), \tag{15}$$

where R_m is measured in bits per second per Hertz, bit/(s·Hz). This formulation explicitly captures the coupling effect between communication and navigation signals and characterizes how the transmit beamformers $w_{k,m}(\boldsymbol{s}_k)$ and $v_k(\boldsymbol{s}_k)$ jointly determine the achievable rate.

2.4 Navigation model

Consider the l^{th} NUE located at position $\boldsymbol{q}_l$. The received signal comprises the desired navigation component, superimposed communication transmissions, and receiver noise. To obtain a satellite-specific navigation observation, the NUE applies a matched filter using the known pseudo-random reference waveform x^{N}_k, which suppresses navigation signals from other satellites. After this satellite-specific matched filtering, by substituting the channel response defined in Eq. (10), the resulting observation at the l^{th} NUE associated with the k^{th} satellite can be written as

$$y^{\text{N}}_{k,l} = \underbrace{\int_{\boldsymbol{S}'_k} h^{\text{N}}_{k,l}(\boldsymbol{s}'_k, \boldsymbol{q}_l)\, v_k(\boldsymbol{s}'_k)\, \mathrm{d}\boldsymbol{s}'_k}_{\text{Desired navigation signal}} + n^{\text{eff}}_{k,l}, \tag{16}$$

where $n^{\text{eff}}_{k,l}$ represents the effective interference-plus-noise term at the l^{th} NUE for the k^{th} satellite after matched filtering, which is given by

$$n^{\text{eff}}_{k,l} = \underbrace{\sum_{k'=1}^{K} \sum_{m=1}^{M} \int_{\boldsymbol{S}'_{k'}} h^{\text{N}}_{k',l}(\boldsymbol{s}'_{k'}, \boldsymbol{q}_l)\, w_{k',m}(\boldsymbol{s}'_{k'})\, \mathrm{d}\boldsymbol{s}'_{k'} \rho'_{k,m}}_{\text{Communication interference}} + n^{\text{N}}_{k,l}. \tag{17}$$

Herein, $\rho'_{k,m} = \langle x^{\text{C}}_m\, x^{\text{N}*}_k \rangle_T$ is the communication residual coefficient after matched filtering, and $n^{\text{N}}_{k,l}$ denotes the AWGN at the l^{th} NUE with zero mean and variance $\sigma^2_{\text{N},l}$.

We adopt a direct position estimation (DPE) framework, where the NUE's position $\boldsymbol{q}_l$ is estimated directly from the received signals (Closas et al., 2009). To fully leverage the geometric diversity provided by the satellite constellation, we model the aggregate received signal as a K-dimensional vector, formed by stacking the distinct observations associated with each satellite:

$$\boldsymbol{y}^{\text{N}}_l = \left[y^{\text{N}}_{1,l},\, y^{\text{N}}_{2,l},\, \ldots,\, y^{\text{N}}_{K,l}\right]^{\text{T}} \in \mathbb{C}^{K\times 1}, \tag{18}$$

which can be compactly expressed as

$$\boldsymbol{y}^{\text{N}}_l = \boldsymbol{\mu}_l(\boldsymbol{q}_l) + \boldsymbol{n}^{\text{eff}}_l, \tag{19}$$

where $\boldsymbol{y}^{\text{N}}_l$ is the observed navigation measurement vector,

$\boldsymbol{\mu}_l(\boldsymbol{q}_l) \in \mathbb{C}^{K\times 1}$ is the position-dependent noise-free mean vector collecting the desired navigation components, and $\boldsymbol{n}_l^{\text{eff}} \in \mathbb{C}^{K\times 1}$ is the effective interference-plus-noise vector. The k^{th} entry of $\boldsymbol{\mu}_l(\boldsymbol{q}_l)$ in Eq. (19) is given by

$$\mu_{k,l}(\boldsymbol{q}_l) = \int_{\boldsymbol{S}'_k} h^{\text{N}}_{k,l}(\boldsymbol{s}'_k, \boldsymbol{q}_l)\, v_k(\boldsymbol{s}'_k)\, \mathrm{d}\boldsymbol{s}'_k, \tag{20}$$

and we have $\boldsymbol{\mu}_l(\boldsymbol{q}_l) = [\mu_{1,l}(\boldsymbol{q}_l), \mu_{2,l}(\boldsymbol{q}_l), \ldots, \mu_{K,l}(\boldsymbol{q}_l)]^{\text{T}}$. Due to the superposition of a large number of independent communication signals after the matched filter, the central limit theorem motivates modeling the aggregate interference as a complex Gaussian process. Consequently, the effective interference-plus-noise term is modeled as

$$\boldsymbol{n}_l^{\text{eff}} \sim \mathcal{CN}\big(\boldsymbol{0}, \sigma^2_{\text{eff},l}\, \boldsymbol{I}_K\big), \tag{21}$$

where $\boldsymbol{I}_K$ is the $K\times K$ identity matrix, and the effective noise variance $\sigma^2_{\text{eff},l}$ is given by

$$\sigma^2_{\text{eff},l} = \eta^{\rho} \sum_{m=1}^{M} \left| \sum_{k=1}^{K} \int_{\boldsymbol{S}'_k} h^{\text{N}}_{k,l}(\boldsymbol{s}'_k, \boldsymbol{q}_l) w_{k,m}(\boldsymbol{s}'_k) \mathrm{d}\boldsymbol{s}'_k \right|^2 + \sigma^2_{\text{N},l}. \tag{22}$$

Herein, $\eta^{\rho} = \mathbb{E}[|\rho'_{k,m}|^2]$ with the assumption that η^{ρ} is identical for all k and m. Based on this model, the probability density function (PDF) of observation $\boldsymbol{y}_l^{\text{N}}$ given position $\boldsymbol{q}_l$ is expressed as (Closas et al., 2007)

$$p(\boldsymbol{y}_l^{\text{N}}|\boldsymbol{q}_l) = \frac{1}{(\pi\sigma^2_{\text{eff},l})^K} \exp\left(-\frac{\left\|\boldsymbol{y}_l^{\text{N}} - \boldsymbol{\mu}_l(\boldsymbol{q}_l)\right\|^2}{\sigma^2_{\text{eff},l}} \right). \tag{23}$$

Derived from Eq. (23), the constant-free negative log-likelihood, which serves as the cost function, is written as

$$\mathcal{L}(\boldsymbol{q}_l) = \frac{\left\|\boldsymbol{y}_l^{\text{N}} - \boldsymbol{\mu}_l(\boldsymbol{q}_l)\right\|^2}{\sigma^2_{\text{eff},l}} + K \ln \sigma^2_{\text{eff},l}. \tag{24}$$

In practice, the dependence of $\sigma^2_{\text{eff},l}$ on position $\boldsymbol{q}_l$ and beamformers is relatively weak compared to that of vector $\boldsymbol{\mu}_l(\boldsymbol{q}_l)$. Following standard practice in deterministic parameter estimation, we adopt an iterative scheme, in which $\sigma^2_{\text{eff},l}$ is updated using the beamformers and the previous position estimate and then treated as a constant within each iteration. The effective noise variance $\sigma^2_{\text{eff},l}$ is not fixed throughout the algorithm, but is recomputed at each outer iteration using the updated beamforming variables and the position estimate. It is only locally frozen within each inner update, so this treatment preserves the effect of residual communication interference on the CRB while neglecting the position derivative of $\sigma^2_{\text{eff},l}$ for tractability. Under this approximation, minimizing $\mathcal{L}(\boldsymbol{q}_l)$ is equivalent to minimizing the squared error term $\left\|\boldsymbol{y}_l^{\text{N}} - \boldsymbol{\mu}_l(\boldsymbol{q}_l)\right\|^2$. To enable gradient-based position refinement, we define the Jacobian matrix of vector $\boldsymbol{\mu}_l$ with respect to position $\boldsymbol{q}_l$ as

$$\boldsymbol{J}_l(\boldsymbol{q}_l) = \frac{\partial \boldsymbol{\mu}_l(\boldsymbol{q}_l)}{\partial \boldsymbol{q}_l^{\text{T}}} = [\nabla_{\boldsymbol{q}_l}\mu_{1,l}(\boldsymbol{q}_l), \ldots, \nabla_{\boldsymbol{q}_l}\mu_{K,l}(\boldsymbol{q}_l)]^{\text{T}}, \tag{25}$$

where the gradient of the k^{th} component is given by

$$\nabla_{\boldsymbol{q}_l}\mu_{k,l}(\boldsymbol{q}_l) = \int_{\boldsymbol{S}'_k} \nabla_{\boldsymbol{q}_l} h^{\text{N}}_{k,l}(\boldsymbol{s}'_k, \boldsymbol{q}_l)\, v_k(\boldsymbol{s}'_k)\, \mathrm{d}\boldsymbol{s}'_k, \tag{26}$$

and the closed-form expression of $\nabla_{\boldsymbol{q}_l} h^{\text{N}}_{k,l}(\boldsymbol{s}'_k, \boldsymbol{q}_l)$ is provided in Appendix A. By using Eq. (25), the gradient of the squared error term is obtained as

$$\nabla_{\boldsymbol{q}_l}\left\|\boldsymbol{y}_l^{\text{N}} - \boldsymbol{\mu}_l(\boldsymbol{q}_l)\right\|^2 = -2\,\Re\Big\{\boldsymbol{J}_l^{\text{H}}(\boldsymbol{q}_l)\big(\boldsymbol{y}_l^{\text{N}} - \boldsymbol{\mu}_l(\boldsymbol{q}_l)\big)\Big\}. \tag{27}$$

Given an initial position estimate $\hat{\boldsymbol{q}}_l^{(0)}$, a gradient-descent-based update can be applied as

$$\hat{\boldsymbol{q}}_l^{(t+1)} = \hat{\boldsymbol{q}}_l^{(t)} - \alpha^{(t)}\nabla_{\boldsymbol{q}_l}\left\|\boldsymbol{y}_l^{\text{N}} - \boldsymbol{\mu}_l(\boldsymbol{q}_l)\right\|^2\Big|_{\boldsymbol{q}_l=\hat{\boldsymbol{q}}_l^{(t)}}, \tag{28}$$

where $\alpha^{(t)} > 0$ denotes the step size at the t^{th} iteration. Once convergence is achieved, the l^{th} NUE can obtain its position $\hat{\boldsymbol{q}}_l$.

To quantify the fundamental limit of positioning accuracy, we employ the CRB as the navigation performance metric, which provides a lower bound on the variance of any unbiased estimator. Under the complex Gaussian observation model, the Fisher information matrix (FIM) with respect to the position vector $\boldsymbol{q}_l$ is given by (Wang ZL et al., 2023)

$$\boldsymbol{F}_l = \frac{2}{\sigma^2_{\text{eff},l}}\,\Re\Big\{\boldsymbol{J}_l^{\text{H}}(\boldsymbol{q}_l)\,\boldsymbol{J}_l(\boldsymbol{q}_l)\Big\}. \tag{29}$$

The CRB matrix is defined as the inverse of the FIM:

$$\mathbf{CRB}(\boldsymbol{q}_l) = \boldsymbol{F}_l^{-1}(\boldsymbol{q}_l). \tag{30}$$

Since the diagonal elements of the CRB matrix correspond to the variance bounds of the individual coordinates, its trace $\mathrm{tr}(\mathbf{CRB}(\boldsymbol{q}_l))$ serves as a scalar metric quantifying the lower bound on the total mean-squared error (MSE) for the l^{th} NUE. Crucially, this expression reveals that the ultimate navigation accuracy is intrinsically coupled with the beamforming design for both communication $w_{k,m}(\boldsymbol{s}_k)$ and navigation $v_k(\boldsymbol{s}_k)$, as these functions determine both the signal gradient and the effective noise variance. Physically, this coupling can be interpreted from two aspects. First, the navigation beamformers $v_k(\boldsymbol{s}'_k)$ determine the desired navigation signal $\boldsymbol{\mu}_l(\boldsymbol{q}_l)$ and its spatial gradient $\boldsymbol{J}_l(\boldsymbol{q}_l)$. A stronger and more position-sensitive navigation field increases the Fisher information and improves the conditioning of $\boldsymbol{F}_l$. Second, the communication beamformers $w_{k,m}(\boldsymbol{s}'_k)$ contribute to the residual interference after matched filtering, as reflected by $\sigma^2_{\text{eff},l}$ in Eq. (22). Since the FIM in Eq. (29) is scaled by $2/\sigma^2_{\text{eff},l}$, stronger communication leakage toward the NUE reduces the effective Fisher information and enlarges the CRB. Therefore, minimizing the CRB under communication rate constraints requires a balance between enhancing the navigation signal gradient and suppressing communication-induced residual interference.

3 Subspace-based CAPA-assisted ICAN beamforming design in LEO satellite constellations

In this section, building on the preceding derivations and analysis, we show that system performance is fully characterized by the spatially continuous source current distributions over the CAPA surfaces of all K serving satellites. In particular, the transmit beamformers for communication $w_{k,m}(\boldsymbol{s}_k)$

and for navigation $v_k(\boldsymbol{s}_k)$ jointly determine the quality delivered to CUE and NUE. Therefore, we present a beamforming design for ICAN to improve the overall performance in LEO satellite constellations.

3.1 Problem formulation

To enhance the overall performance of a dual-function LEO satellite constellation, we minimize the average trace of the CRB for position estimation while simultaneously guaranteeing a minimum achievable rate for all CUEs and satisfying the per-satellite maximum transmit power constraints on each CAPA surface by optimizing the transmit beamformers. The optimization problem is mathematically stated as follows:

$$\min_{\{w_{k,m}\},\{v_k\}} \quad \frac{1}{L}\sum_{l=1}^{L} \mathrm{tr}\left(\mathbf{CRB}(\boldsymbol{q}_l)\right) \tag{31a}$$

$$\text{s.t.} \quad \log_2(1+\gamma_m) \geq R_m^{\min}, \tag{31b}$$

$$\int_{\boldsymbol{S}'_k}\left(\sum_{m=1}^{M}|w_{k,m}(\boldsymbol{s}'_k)|^2+|v_k(\boldsymbol{s}'_k)|^2\right)\mathrm{d}\boldsymbol{s}'_k \leq P_k^{\max}. \tag{31c}$$

In this formulation, the objective function (31a) seeks to minimize the average positioning error bound across all NUEs. The constraint (31b) based on Eq. (15) ensures that each CUE attains its required minimum quality-of-service (QoS) threshold with $R_m^{\min}$ being the required minimum achievable rate. The constraint (31c) derived from Eq. (5) enforces a per-satellite transmit power limit at the CAPA surface with $P_k^{\max}$ being the current factor proportional to the maximum transmit power budget. Therefore, problem (31) can be regarded as a multi-objective optimization problem for CAPA-assisted ICAN, where navigation accuracy and communication QoS are jointly considered. Specifically, the average CRB is minimized to improve navigation performance, while the achievable-rate requirements of all CUEs are explicitly imposed to guarantee communication performance. It is worth noting that the primary challenge in solving problem (31) stems from its infinite-dimensional nature, since the optimization variables are functions defined over the continuous domain of the CAPA surfaces. To render this problem tractable, it is necessary to transform it into a finite-dimensional equivalent without sacrificing optimality. Moreover, the quadratic terms in the optimization variables and the cross-coupling induced by the dual-function design render problem (31) non-convex and generally intractable, so an exact optimal solution cannot be obtained in polynomial time. In this context, we develop an efficient algorithm that obtains feasible suboptimal solutions and improves the overall performance of the CAPA-assisted ICAN system in LEO satellite constellations. The subsequent subsections focus on a dimensionality-reduction transformation of the problem and the corresponding algorithm design.

3.2 Channel subspace transformation

Because the optimization variables are defined over continuous surfaces $\boldsymbol{S}'_k$, we adopt a channel subspace-based approach projecting the infinite-dimensional problem onto a finite-dimensional subspace without loss of optimality (Zhao JJ et al., 2025). The key to dimensionality reduction is to restrict the search space of the transmit beamformers to a properly constructed joint communication and navigation channel subspace.

Theorem 1 Define the finite-dimensional ICAN channel subspace for the k^{th} satellite, spanned by the basis functions given by the conjugates of the continuous communication and navigation channel responses associated with the CAPA surface:

$$\mathcal{C}_k \triangleq \mathrm{span}\left(\{h_{k,m}^{\mathrm{C}}(\boldsymbol{s}'_k,\boldsymbol{p}_m)^*\}_{m=1}^{M} \cup \{h_{k,l}^{\mathrm{N}}(\boldsymbol{s}'_k,\boldsymbol{q}_l)^*\}_{l=1}^{L}\right), \tag{32}$$

where $\mathrm{span}(\cdot)$ denotes the set of all functions formed by finite linear combinations of the listed basis functions. Then, there exists an optimal solution to problem (31) whose transmit beamformers satisfy $w_{k,m}(\boldsymbol{s}'_k) \in \mathcal{C}_k$ for all m values and $v_k(\boldsymbol{s}'_k) \in \mathcal{C}_k$.

Proof See Appendix B.

According to Theorem 1, an optimal set of transmit beamformers $w_{k,m}(\boldsymbol{s}'_k)$ and $v_k(\boldsymbol{s}'_k)$ can be chosen to lie entirely within $\mathcal{C}_k$, denoted as

$$\begin{aligned} w_{k,m}(\boldsymbol{s}'_k) &= \sum_{m'=1}^{M}\alpha_{k,m,m'}^{\mathrm{C}}\, h_{k,m'}^{\mathrm{C}}(\boldsymbol{s}'_k,\boldsymbol{p}_{m'})^* + \sum_{l'=1}^{L}\beta_{k,m,l'}^{\mathrm{C}}\, h_{k,l'}^{\mathrm{N}}(\boldsymbol{s}'_k,\boldsymbol{q}_{l'})^* \\ &= \boldsymbol{\Phi}_k^{\mathrm{T}}(\boldsymbol{s}'_k)\,\boldsymbol{a}_{k,m}, \end{aligned} \tag{33}$$

$$\begin{aligned} v_k(\boldsymbol{s}'_k) &= \sum_{m=1}^{M}\alpha_{k,m}^{\mathrm{N}}\, h_{k,m}^{\mathrm{C}}(\boldsymbol{s}'_k,\boldsymbol{p}_m)^* + \sum_{l=1}^{L}\beta_{k,l}^{\mathrm{N}}\, h_{k,l}^{\mathrm{N}}(\boldsymbol{s}'_k,\boldsymbol{q}_l)^* \\ &= \boldsymbol{\Phi}_k^{\mathrm{T}}(\boldsymbol{s}'_k)\,\boldsymbol{b}_k, \end{aligned} \tag{34}$$

where $\boldsymbol{a}_{k,m} = \left[\alpha_{k,m,1}^{\mathrm{C}},\alpha_{k,m,2}^{\mathrm{C}},\ldots,\alpha_{k,m,M}^{\mathrm{C}},\beta_{k,m,1}^{\mathrm{C}},\beta_{k,m,2}^{\mathrm{C}},\ldots,\beta_{k,m,L}^{\mathrm{C}}\right]^{\mathrm{T}} \in \mathbb{C}^{(M+L)\times 1}$, $\boldsymbol{b}_k = \left[\alpha_{k,1}^{\mathrm{N}},\alpha_{k,2}^{\mathrm{N}},\ldots,\alpha_{k,M}^{\mathrm{N}},\beta_{k,1}^{\mathrm{N}},\beta_{k,2}^{\mathrm{N}},\ldots,\beta_{k,L}^{\mathrm{N}}\right]^{\mathrm{T}} \in \mathbb{C}^{(M+L)\times 1}$, and the subspace basis vector $\boldsymbol{\Phi}_k(\boldsymbol{s}'_k)$ for the k^{th} satellite is denoted as

$$\begin{aligned} \boldsymbol{\Phi}_k(\boldsymbol{s}'_k) = \Big[& h_{k,1}^{\mathrm{C}}(\boldsymbol{s}'_k,\boldsymbol{p}_1)^*,\ h_{k,2}^{\mathrm{C}}(\boldsymbol{s}'_k,\boldsymbol{p}_2)^*,\ \ldots, h_{k,M}^{\mathrm{C}}(\boldsymbol{s}'_k,\boldsymbol{p}_M)^*, \\ & h_{k,1}^{\mathrm{N}}(\boldsymbol{s}'_k,\boldsymbol{q}_1)^*,\ h_{k,2}^{\mathrm{N}}(\boldsymbol{s}'_k,\boldsymbol{q}_2)^*,\ \ldots, h_{k,L}^{\mathrm{N}}(\boldsymbol{s}'_k,\boldsymbol{q}_L)^*\Big]^{\mathrm{T}} \\ & \in \mathbb{C}^{(M+L)\times 1}. \end{aligned} \tag{35}$$

Herein, $\alpha_{k,m,m'}^{\mathrm{C}}$ and $\beta_{k,m,l'}^{\mathrm{C}}$ are the expansion coefficients of the communication transmit beamformer $w_{k,m}$ on the conjugate communication and navigation channel bases, respectively, and $\alpha_{k,m}^{\mathrm{N}}$ and $\beta_{k,l}^{\mathrm{N}}$ are the corresponding coefficients of the navigation transmit beamformer v_k.

By leveraging the subspace transformation, the infinite-dimensional optimization variables $w_{k,m}(\boldsymbol{s}'_k)$ and $v_k(\boldsymbol{s}'_k)$ are parameterized by the finite-dimensional coefficient vectors $\boldsymbol{a}_{k,m}$ and $\boldsymbol{b}_k$, respectively. In this context, by substituting Eqs. (33) and (34) into Eqs. (11) and (16), the received signals at the m^{th} CUE and the l^{th} NUE can be rewritten as

$$y_m^{\mathrm{C}} = \sum_{k=1}^{K}\left(\boldsymbol{g}_{k,m}^{\mathrm{C}}\boldsymbol{a}_{k,m}x_m^{\mathrm{C}} + \sum_{i=1,i\neq m}^{M}\boldsymbol{g}_{k,m}^{\mathrm{C}}\boldsymbol{a}_{k,i}x_i^{\mathrm{C}} + \boldsymbol{g}_{k,m}^{\mathrm{C}}\boldsymbol{b}_k x_k^{\mathrm{N}}\right) + n_m^{\mathrm{C}}, \tag{36}$$

$$y_{k,l}^{\mathrm{N}} = \boldsymbol{g}_{k,l}^{\mathrm{N}}\boldsymbol{b}_k + \sum_{k'=1}^{K}\sum_{m=1}^{M}\boldsymbol{g}_{k',l}^{\mathrm{N}}\boldsymbol{a}_{k',m}\rho'_{k,m} + n_{k,l}^{\mathrm{N}}, \tag{37}$$

where $\boldsymbol{g}_{k,m}^{\mathrm{C}} \in \mathbb{C}^{1\times(M+L)}$ and $\boldsymbol{g}_{k,l}^{\mathrm{N}} \in \mathbb{C}^{1\times(M+L)}$ denote the effective subspace channel vectors from the k^{th} satellite to the m^{th} CUE and to the l^{th} NUE, respectively, defined as

$$\boldsymbol{g}_{k,m}^{\mathrm{C}} = \int_{\boldsymbol{S}'_k} h_{k,m}^{\mathrm{C}}(\boldsymbol{s}'_k, \boldsymbol{p}_m)\, \boldsymbol{\varPhi}_k^{\mathrm{T}}(\boldsymbol{s}'_k)\, \mathrm{d}\boldsymbol{s}'_k, \tag{38}$$

$$\boldsymbol{g}_{k,l}^{\mathrm{N}} = \int_{\boldsymbol{S}'_k} h_{k,l}^{\mathrm{N}}(\boldsymbol{s}'_k, \boldsymbol{q}_l)\, \boldsymbol{\varPhi}_k^{\mathrm{T}}(\boldsymbol{s}'_k)\, \mathrm{d}\boldsymbol{s}'_k. \tag{39}$$

In addition, this dimensionality-reduction transformation allows us to reformulate the original problem (31) into a tractable form. First, we focus on the CRB matrix in the objective function (31a), which depends on the desired navigation signal component and its spatial gradient at each NUE. After the channel subspace transformation in Eqs. (33) and (34), $\mu_l(\boldsymbol{q}_l)$ and $\nabla_{\boldsymbol{q}_l}\mu_l(\boldsymbol{q}_l)$ can be re-expressed in terms of $\boldsymbol{b}_k$ as

$$\mu_{k,l}(\boldsymbol{q}_l) = \boldsymbol{g}_{k,l}^{\mathrm{N}}\boldsymbol{b}_k, \tag{40}$$

$$\nabla_{\boldsymbol{q}_l}\mu_{k,l}(\boldsymbol{q}_l) = \boldsymbol{D}_{k,l}(\boldsymbol{q}_l)\boldsymbol{b}_k, \tag{41}$$

where

$$\boldsymbol{D}_{k,l}(\boldsymbol{q}_l) = \int_{\boldsymbol{S}'_k} \nabla_{\boldsymbol{q}_l} h_{k,l}^{\mathrm{N}}(\boldsymbol{s}'_k, \boldsymbol{q}_l)\boldsymbol{\varPhi}_k^{\mathrm{T}}(\boldsymbol{s}'_k)\mathrm{d}\boldsymbol{s}'_k. \tag{42}$$

Moreover, the effective noise variance at the l^{th} NUE $\sigma_{\mathrm{eff},l}^2$ can be rewritten as

$$\sigma_{\mathrm{eff},l}^2 = \eta^{\rho}\sum_{m=1}^{M}\left|\sum_{k=1}^{K}\boldsymbol{g}_{k,l}^{\mathrm{N}}\boldsymbol{a}_{k,m}\right|^2 + \sigma_{\mathrm{N},l}^2. \tag{43}$$

Similarly, the communication achievable rate constraint (31b) and the transmit power constraint (31c) can be rewritten as

$$\frac{\left|\sum\limits_{k=1}^{K}\boldsymbol{g}_{k,m}^{\mathrm{C}}\boldsymbol{a}_{k,m}\right|^2}{\sum\limits_{i=1,i\neq m}^{M}\left|\sum\limits_{k=1}^{K}\boldsymbol{g}_{k,m}^{\mathrm{C}}\boldsymbol{a}_{k,i}\right|^2 + \sum\limits_{k=1}^{K}\left|\boldsymbol{g}_{k,m}^{\mathrm{C}}\boldsymbol{b}_k\right|^2 + \sigma_{\mathrm{C},m}^2} \geq \varGamma_m, \tag{44}$$

$$\sum_{m=1}^{M}\boldsymbol{a}_{k,m}^{\mathrm{H}}\boldsymbol{R}_k^{\mathrm{P}}\boldsymbol{a}_{k,m} + \boldsymbol{b}_k^{\mathrm{H}}\boldsymbol{R}_k^{\mathrm{P}}\boldsymbol{b}_k \leq P_k^{\max}, \tag{45}$$

where $\varGamma_m = 2^{R_m^{\min}} - 1$ and $\boldsymbol{R}_k^{\mathrm{P}} = \int_{\boldsymbol{S}'_k}\boldsymbol{\varPhi}_k(\boldsymbol{s}'_k)\boldsymbol{\varPhi}_k^{\mathrm{H}}(\boldsymbol{s}'_k)\mathrm{d}\boldsymbol{s}'_k \in \mathbb{C}^{(M+L)\times(M+L)}$. In this context, the original infinite-dimensional problem (31) is reformulated as an equivalent finite-dimensional optimization problem over the coefficient vectors $\boldsymbol{a}_{k,m}$ and $\boldsymbol{b}_k$, which can be expressed as

$$\min_{\{\boldsymbol{a}_{k,m}\},\{\boldsymbol{b}_k\}} \quad \frac{1}{L}\sum_{l=1}^{L}\mathrm{tr}\left(\mathbf{CRB}(\boldsymbol{q}_l)\right) \tag{46a}$$

$$\text{s.t.} \quad \text{constraints (44) and (45).} \tag{46b}$$

After the channel subspace transformation, problem (46) is cast into a finite-dimensional form but remains non-convex due to the complicated objective function, the quadratic terms, and the coupling among the optimization variables.

3.3 Algorithm design

To address this non-convexity, we apply the semi-definite relaxation (SDR) technique and define matrices $\boldsymbol{A}_m = \boldsymbol{a}_m\boldsymbol{a}_m^{\mathrm{H}}$ and $\boldsymbol{B} = \boldsymbol{b}\boldsymbol{b}^{\mathrm{H}}$, where $\boldsymbol{a}_m = [\boldsymbol{a}_{1,m}^{\mathrm{T}}, \boldsymbol{a}_{2,m}^{\mathrm{T}}, \ldots, \boldsymbol{a}_{K,m}^{\mathrm{T}}]^{\mathrm{T}}$ and $\boldsymbol{b} = [\boldsymbol{b}_1^{\mathrm{T}}, \boldsymbol{b}_2^{\mathrm{T}}, \ldots, \boldsymbol{b}_K^{\mathrm{T}}]^{\mathrm{T}}$ are aggregate vectors by stacking the expansion coefficients for all K satellites. Accordingly, the communication achievable rate constraint (44) is rewritten as

$$\mathrm{tr}(\boldsymbol{G}_m^{\mathrm{C}}\boldsymbol{A}_m) \geq \varGamma_m\left(\sum_{i=1,i\neq m}^{M}\mathrm{tr}(\boldsymbol{G}_m^{\mathrm{C}}\boldsymbol{A}_i) + \mathrm{tr}(\tilde{\boldsymbol{G}}_m^{\mathrm{C}}\boldsymbol{B}) + \sigma_{\mathrm{C},m}^2\right), \tag{47}$$

where the communication channel matrices $\boldsymbol{G}_m^{\mathrm{C}} \in \mathbb{C}^{K(M+L)\times K(M+L)}$ and $\tilde{\boldsymbol{G}}_m^{\mathrm{C}} \in \mathbb{C}^{K(M+L)\times K(M+L)}$ for the m^{th} CUE are defined as

$$\boldsymbol{G}_m^{\mathrm{C}} = \boldsymbol{g}_m^{\mathrm{C}}(\boldsymbol{g}_m^{\mathrm{C}})^{\mathrm{H}}, \tag{48}$$

$$\tilde{\boldsymbol{G}}_m^{\mathrm{C}} = \mathrm{blkdiag}\left(\boldsymbol{g}_{1,m}^{\mathrm{C}}(\boldsymbol{g}_{1,m}^{\mathrm{C}})^{\mathrm{H}}, \boldsymbol{g}_{2,m}^{\mathrm{C}}(\boldsymbol{g}_{2,m}^{\mathrm{C}})^{\mathrm{H}}, \ \ldots, \boldsymbol{g}_{K,m}^{\mathrm{C}}(\boldsymbol{g}_{K,m}^{\mathrm{C}})^{\mathrm{H}}\right), \tag{49}$$

with $\boldsymbol{g}_m^{\mathrm{C}} = \left[\boldsymbol{g}_{1,m}^{\mathrm{C}}, \boldsymbol{g}_{2,m}^{\mathrm{C}}, \cdots, \boldsymbol{g}_{K,m}^{\mathrm{C}}\right]^{\mathrm{T}} \in \mathbb{C}^{K(M+L)\times 1}$. Similarly, the transmit power constraint (45) is updated as

$$\sum_{m=1}^{M}\mathrm{tr}(\tilde{\boldsymbol{R}}_k^{\mathrm{P}}\boldsymbol{A}_m) + \mathrm{tr}(\tilde{\boldsymbol{R}}_k^{\mathrm{P}}\boldsymbol{B}) \leq P_k^{\max}, \tag{50}$$

where $\tilde{\boldsymbol{R}}_k^{\mathrm{P}} = \mathrm{blkdiag}(\boldsymbol{0}, \ \ldots, \boldsymbol{R}_k^{\mathrm{P}}, \ \ldots, \boldsymbol{0}) \in \mathbb{C}^{K(M+L)\times K(M+L)}$ is a block-diagonal selector matrix whose k^{th} diagonal block is matrix $\boldsymbol{R}_k^{\mathrm{P}}$ and all other blocks are zero, thus acting as a selector that isolates the power contribution of the k^{th} satellite only.

Furthermore, the CRB-based objective function (46a) is the most challenging component to handle. To facilitate its reformulation, we define the navigation channel matrix for the l^{th} NUE as $\boldsymbol{G}_l^{\mathrm{N}} = \boldsymbol{g}_l^{\mathrm{N}}(\boldsymbol{g}_l^{\mathrm{N}})^{\mathrm{H}}$, where the aggregated subspace channel vector for the l^{th} NUE is given by $\boldsymbol{g}_l^{\mathrm{N}} = [\boldsymbol{g}_{1,l}^{\mathrm{N}}, \boldsymbol{g}_{2,l}^{\mathrm{N}}, \cdots, \boldsymbol{g}_{K,l}^{\mathrm{N}}]^{\mathrm{T}} \in \mathbb{C}^{K(M+L)\times 1}$. According to Eqs. (25), (29), (30), (41), and (43), the objective function (46a) can be rewritten as (51) in terms of the matrix variables $\{\boldsymbol{A}_m\}$ and $\boldsymbol{B}$ at the top of the next page, where $\sigma_{\mathrm{eff},l}^2$ is transformed into

$$\sigma_{\mathrm{eff},l}^2 = \eta^{\rho}\sum_{m=1}^{M}\mathrm{tr}(\boldsymbol{G}_l^{\mathrm{N}}\boldsymbol{A}_m) + \sigma_{\mathrm{N},l}^2, \tag{52}$$

and $\boldsymbol{E}_k \in \mathbb{R}^{(M+L)\times K(M+L)}$ is a block selection matrix defined as $\boldsymbol{E}_k = [\boldsymbol{0}, \ldots, \boldsymbol{I}_{M+L}, \ldots, \boldsymbol{0}]$, with the identity block $\boldsymbol{I}_{M+L}$ placed at the k^{th} block position, thereby selecting the coefficients corresponding to the k^{th} satellite. To avoid explicit matrix inversion in the object function (51), we introduce an auxiliary variable matrix $\boldsymbol{T}_l \succeq 0$ with $\boldsymbol{T}_l \succeq \frac{2}{\sigma_{\mathrm{eff},l}^2}\Re\{\sum_{k=1}^{K}\boldsymbol{D}_{k,l}(\boldsymbol{q}_l)\,\boldsymbol{E}_k\boldsymbol{B}\boldsymbol{E}_k^{\mathrm{H}}\,\boldsymbol{D}_{k,l}^{\mathrm{H}}(\boldsymbol{q}_l)\}$. According to the Schur complement theorem, the objective function (51) is equivalently reformulated as minimizing $\frac{1}{L}\sum_{l=1}^{L}\mathrm{tr}\left(\boldsymbol{T}_l\right)$, which is subject to

$$\begin{bmatrix} \boldsymbol{T}_l & \boldsymbol{I}_3 \\ \boldsymbol{I}_3 & \frac{2}{\sigma_{\mathrm{eff},l}^2}\Re\left\{\sum\limits_{k=1}^{K}\boldsymbol{D}_{k,l}(\boldsymbol{q}_l)\,\boldsymbol{E}_k\boldsymbol{B}\boldsymbol{E}_k^{\mathrm{H}}\,\boldsymbol{D}_{k,l}^{\mathrm{H}}(\boldsymbol{q}_l)\right\} \end{bmatrix} \succeq 0. \tag{53}$$

Consequently, the original optimization problem (46) can

$$\min_{\{\boldsymbol{A}_m\},\boldsymbol{B}} \frac{1}{L}\sum_{l=1}^{L} \operatorname{tr}\left(\left(\frac{2}{\sigma_{\text{eff},l}^2}\Re\left\{\sum_{k=1}^{K} \boldsymbol{D}_{k,l}(\boldsymbol{q}_l)\,\boldsymbol{E}_k\boldsymbol{B}\boldsymbol{E}_k^{\mathrm{H}}\,\boldsymbol{D}_{k,l}^{\mathrm{H}}(\boldsymbol{q}_l)\right\}\right)^{-1}\right). \tag{51}$$

be reformulated as

$$\min_{\{\boldsymbol{A}_m\},\boldsymbol{B},\{\boldsymbol{T}_l\}} \quad \frac{1}{L}\sum_{l=1}^{L}\operatorname{tr}\left(\boldsymbol{T}_l\right) \tag{54a}$$

$$\text{s.t.} \quad \text{constraints (47), (50), and (53)},$$

$$\boldsymbol{A}_m \succeq 0, \quad \boldsymbol{B} \succeq 0, \tag{54b}$$

$$\operatorname{Rank}\left(\boldsymbol{A}_m\right)=1, \quad \operatorname{Rank}\left(\boldsymbol{B}\right)=1, \tag{54c}$$

where constraint (53) is still non-convex because $\sigma_{\text{eff},l}^2$ depends on $\boldsymbol{A}_m$, which in turn induces coupling between optimize variables $\boldsymbol{A}_m$ and $\boldsymbol{B}$. To solve this problem, we apply a block coordinate descent (BCD) method by fixing $\sigma_{\text{eff},l}^2$ at each iteration to its value from the previous step, denoted by $\sigma_{\text{eff},l}^{2,(t-1)}$, so that inequality (53) becomes a standard linear matrix inequality (LMI). In particular, a damped update strategy is employed to improve stability:

$$\sigma_{\text{eff},l}^{2,(t)} = (1-\lambda')\sigma_{\text{eff},l}^{2,(t-1)} + \lambda'\sigma_{\text{eff},l}^{2,\text{new}}, \tag{55}$$

where $\lambda' \in (0,1)$ is a damping factor that controls the update step size and helps avoid large oscillations of the objective value across iterations, and $\sigma_{\text{eff},l}^{2,\text{new}}$ denotes the effective noise variance recomputed from the current solution $\boldsymbol{A}_m^{(t)}$. In addition, the positive semi-definite constraint (54b) and non-convex rank-one constraint (54c) arise from the application of the SDR technique. To handle the non-convex rank-one constraints in constraint (54c), we employ a penalty-based successive convex approximation (SCA) method. The detailed derivation of this penalty-based SCA approximation is provided in Appendix C. By combining the BCD method for handling the coupling in constraint (53) and the SCA-based penalty method to enforce the rank-one constraint (54c), we arrive at an iterative optimization algorithm. In the t^{th} iteration, the resulting subproblem can be written as the following convex problem, where ρ is a penalty factor:

$$\min_{\substack{\{\boldsymbol{A}_m\},\boldsymbol{B},\\ \{\boldsymbol{T}_l\}}} \frac{1}{L}\sum_{l=1}^{L}\operatorname{tr}(\boldsymbol{T}_l)+\rho\Bigg(\sum_{m=1}^{M}\left(\operatorname{tr}(\boldsymbol{A}_m)-\left(\boldsymbol{u}_{\boldsymbol{A}_m}^{(t-1)}\right)^{\mathrm{H}}\boldsymbol{A}_m\boldsymbol{u}_{\boldsymbol{A}_m}^{(t-1)}\right)$$

$$+\operatorname{tr}(\boldsymbol{B})-\left(\boldsymbol{u}_{\boldsymbol{B}}^{(t-1)}\right)^{\mathrm{H}}\boldsymbol{B}\boldsymbol{u}_{\boldsymbol{B}}^{(t-1)}\Bigg) \tag{56a}$$

$$\text{s.t.} \quad \text{constraints (47), (50), and (54b)},$$

$$\begin{bmatrix} \boldsymbol{T}_l & \boldsymbol{I}_3 \\ \boldsymbol{I}_3 & \frac{2}{\sigma_{\text{eff},l}^{2,(t-1)}}\Re\left\{\sum\limits_{k=1}^{K}\boldsymbol{D}_{k,l}(\boldsymbol{q}_l)\,\boldsymbol{E}_k\boldsymbol{B}\boldsymbol{E}_k^{\mathrm{H}}\,\boldsymbol{D}_{k,l}^{\mathrm{H}}(\boldsymbol{q}_l)\right\}\end{bmatrix} \succeq 0. \tag{56b}$$

This problem is a standard semi-definite programming (SDP) formulation, which can be solved efficiently using existing convex optimization toolboxes. After obtaining the solutions $\boldsymbol{A}_m^{(t)}$ and $\boldsymbol{B}^{(t)}$, the effective noise variance $\sigma_{\text{eff},l}^{2,(t)}$ and the principal eigenvectors $\boldsymbol{u}_{\boldsymbol{A}_m}^{(t)}$ and $\boldsymbol{u}_{\boldsymbol{B}}^{(t)}$ are updated for the next iteration. If the final solutions are not perfectly rank-one, a standard Gaussian randomization procedure can be applied to extract a high-quality rank-one approximate solution. Once the algorithm converges to the final optimal solutions $\boldsymbol{A}_m^*$ and $\boldsymbol{B}^*$ from the iteration process of solving problem (56), the transmit beamformers for communication and navigation at each satellite's CAPA in the original problem (31) can be calculated as

$$w_{k,m}^*(\boldsymbol{s}_k') = \boldsymbol{\Phi}_k^{\mathrm{T}}(\boldsymbol{s}_k')\boldsymbol{E}_k\left(\sqrt{\lambda_{\max}(\boldsymbol{A}_m^*)}\,\boldsymbol{u}_{\boldsymbol{A}_m^*}\right), \tag{57}$$

$$v_k^*(\boldsymbol{s}_k') = \boldsymbol{\Phi}_k^{\mathrm{T}}(\boldsymbol{s}_k')\boldsymbol{E}_k\left(\sqrt{\lambda_{\max}(\boldsymbol{B}^*)}\,\boldsymbol{u}_{\boldsymbol{B}^*}\right), \tag{58}$$

where $\boldsymbol{u}_{\boldsymbol{A}_m^*}$ and $\boldsymbol{u}_{\boldsymbol{B}^*}$ denote the unit-norm principal eigenvectors associated with $\lambda_{\max}(\boldsymbol{A}_m^*)$ and $\lambda_{\max}(\boldsymbol{B}^*)$, respectively. $\lambda_{\max}(\cdot)$ denotes the maximum eigenvalue. To summarize, the overall procedure of the proposed subspace-based beamforming design for the CAPA-assisted ICAN system in LEO satellite constellations is presented in Algorithm 1.

Algorithm 1 Subspace-based CAPA-assisted ICAN beamforming design in LEO satellite constellations

Input: $K, M, L, D_x, D_y, R_m^{\min}, P_k^{\max}, \boldsymbol{r}_k, \boldsymbol{p}_m, \boldsymbol{q}_l, \rho, \lambda', \varrho, \iota$
// ϱ is the penalty threshold and ι is the penalty scaling factor
Output: $w_{k,m}^*, v_k^*$

```
Initialize iteration index t = 1 and the initial feasible points A_m^(0) and B^(0)
repeat
    update σ_eff,l^{2,(t-1)} according to Eq. (55)
    update principal eigenvectors u_{A_m}^(t-1) and u_B^(t-1) via the eigenvalue decomposition method
    obtain A_m^(t) and B^(t) by solving problem (56)
    if A_m^(t) and B^(t) converge then
        if Σ_{m=1}^{M} |(tr(A_m^(t)) − λ_max(A_m^(t)))| + |tr(B^(t)) − λ_max(B^(t))| > ϱ then
            update the penalty factor ρ = ιρ
        end if
    end if
    update t = t + 1
until convergence
obtain w*_{k,m} and v*_k by eigenvalue decomposition and matrix operations according to Eqs. (57) and (58)
```

3.4 Algorithm analysis

In the following, we analyze in detail the convergence behavior and computational complexity of the proposed algorithm.

1. Convergence analysis. For the proposed Algorithm 1, which iteratively solves the convex SDP in problem (56) to update $\boldsymbol{A}_m$ and $\boldsymbol{B}$, the objective value of the penalized problem is monotonically non-increasing. Specifically, let $\mathcal{J}^{(t)}$ denote the objective value of problem (56) at the t^{th} iteration. Since formulation (56) is a convex SDP problem that is optimally solved at each iteration for fixed $\sigma_{\text{eff},l}^{2,(t-1)}$, $\boldsymbol{u}_{\boldsymbol{A}_m}^{(t-1)}$, and $\boldsymbol{u}_{\boldsymbol{B}}^{(t-1)}$, we have

$\mathcal{J}^{(t)} \leq \mathcal{J}^{(t-1)}$ $\forall t$. Moreover, the feasible set defined by the achievable rate constraint (47), transmit power constraint (50), and LMI constraint (56b) is compact, which guarantees that $\mathcal{J}^{(t)}$ is bounded below. Hence, the sequence $\mathcal{J}^{(t)}$ converges by the monotone bounded criterion (Zorich and Paniagua, 2016). In addition, according to standard results on BCD and SCA, any limit point of the generated sequence $\{\boldsymbol{A}_m^{(t)}, \boldsymbol{B}^{(t)}, \boldsymbol{T}_l^{(t)}\}$ satisfies the Karush–Kuhn–Tucker (KKT) conditions of the penalized SDR problem, and thus corresponds to a stationary solution of the original beamforming design.

2. Complexity analysis. The computational complexity of Algorithm 1 is dominated by solving the convex SDP in problem (56) at each iteration. Other updates, such as $\sigma_{\mathrm{eff},l}^{2,(t)}$ and eigenvector extractions, incur negligible costs. Let $N_\mathrm{b} = M + L$ denote the per-satellite subspace dimension and $N_\mathrm{s} = KN_\mathrm{b}$ denote the aggregate dimension. In problem (56), $\boldsymbol{A}_m$ and $\boldsymbol{B}$ are Hermitian positive semidefinite matrices of size $N_\mathrm{s} \times N_\mathrm{s}$, and $\{\boldsymbol{T}_l\}_{l=1}^{L}$ are Hermitian 3×3 matrices. The number of decision variables is on the order of $\varsigma = \mathcal{O}\big((M+1)N_\mathrm{s}^2 + 9L\big)$. Since problem (56) is a standard SDP problem with LMI constraints, it can be efficiently solved by an interior-point method. Problem (56) includes $(M+1)$ LMI constraints of dimension N_s associated with $\boldsymbol{A}_m \succeq 0$ and $\boldsymbol{B} \succeq 0$ and L LMI constraints of dimension 6 arising from constraint (56b), together with additional scalar linear constraints. Therefore, the overall barrier parameter is approximately

$$\nu = \mathcal{O}\big((M+1)N_\mathrm{s} + 6L\big). \tag{59}$$

Following Wang KY et al. (2014), the worst-case arithmetic complexity of solving problem (56) to accuracy $\zeta > 0$ in one iteration is given by

$$\mathcal{C}_\mathrm{iter} = \mathcal{O}\big(\sqrt{\nu}\,\varXi \ln(1/\zeta)\big), \tag{60}$$

where $\varXi$ is a polynomial in the problem dimensions and can be upper bounded by

$$\varXi = \varsigma\Big[(M+1)N_\mathrm{s}^3 + 216L + \varsigma\big((M+1)N_\mathrm{s}^2 + 36L\big) + \varsigma^2\Big]. \tag{61}$$

Consequently, the overall complexity of Algorithm 1 is given by the following equation with I_iter denoting the number of outer iterations:

$$\mathcal{C}_\mathrm{total} = \mathcal{O}\big(I_\mathrm{iter}\sqrt{\nu}\,\varXi \ln(1/\zeta)\big), \tag{62}$$

which grows polynomially with K, M, and N_b and is typical for SDP-based beamforming designs. The dependence on K, M, and L is explicitly reflected in the SDP structure of problem (56), namely, the number of positive semidefinite matrix variables, their matrix dimensions, and the number of CRB-related LMI constraints, which jointly determine ς, ν, and $\varXi$ in the above expressions. In addition, the convergence and performance trends under representative values of K, M, and L will be further illustrated in Section 4.

4 Simulation results

This section describes the simulation setup and presents numerical results to demonstrate the effectiveness of the proposed algorithm. Without loss of generality, we consider a classical Walker Delta LEO satellite constellation similar to the Starlink system (Al-Hourani, 2021). The constellation is configured with an orbital altitude of $h^* = 550$ km, consisting of $P^* = 72$ orbital planes, with $N^* = 18$ satellites per plane, an inclination of $i^* = 53°$, and a phase factor of $F^* = 45$. In all simulations, a subset of satellites is selected from this constellation as the service group according to an elevation–angle priority rule. Specifically, for a given observation point, all visible satellites above the local horizon are first identified, and the K satellites with the largest elevation angles are selected to form the cooperative service group. This selection rule favors satellites with shorter propagation distances and more favorable link geometries, which is beneficial for both cooperative downlink transmission and navigation signal reception. To illustrate the resulting satellite geometry, Fig. 2 shows the local skyplot of the selected service-group satellites for the case with $K = 5$, where the observation point is located at $[6371, 0, 0]^\mathrm{T}$ km in the ECEF coordinate system.

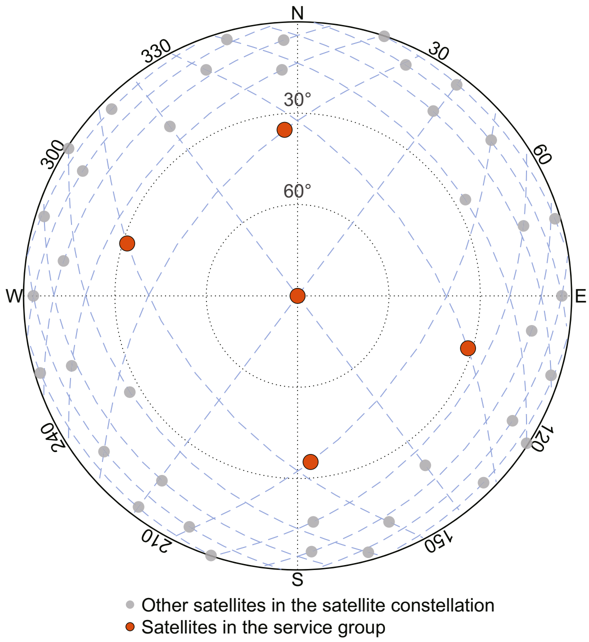

Fig. 2 Skyplot of the service group satellites in the Walker Delta constellation

In this skyplot, the angular coordinate represents the azimuth angle, while the radial coordinate represents the elevation angle. Therefore, satellites closer to the center of the skyplot have higher elevation angles and are selected with higher priority for cooperative ICAN transmission. Satellite layout affects the CRB through LoS diversity. Wider azimuth/elevation separation makes the position gradients in $\boldsymbol{J}_l(\boldsymbol{q}_l)$ less correlated and improves the FIM conditioning, whereas clustered satellites may suffer from poor geometric diversity. Furthermore, the CUEs and NUEs are assumed to be randomly distributed within a 30-km radius around this observation point. All integral evaluations in the simulations are performed using a 10-point Gauss–Legendre scheme (Olver et al., 2010). The effective radiating area of the CAPAs is set to $A_T = 0.25$ m^2 with side lengths $D_x = D_y = \sqrt{A_T}$. The noise variance is set to $\sigma_{\mathrm{C},m}^2 = \sigma_{\mathrm{N},l}^2 = 5.6 \times 10^{-3}$ V^2/m^2. The algorithmic parameters in Algorithm 1 are selected according to penalty-based iterative optimization principles. Specifically, $\rho = 1$ balances the CRB objective and the rank-one penalty, $\lambda' = 0.2$ stabilizes the update of $\sigma^2_{\mathrm{eff},l}$, $\varrho = 10^{-3}$ controls the rank-one residual, and $\iota = 1.2$ gradually strengthens the penalty factor. From a sensitivity perspective, these parameters mainly influence the convergence behavior and rank-one recovery of Algorithm 1. Among them, λ' and ρ are the two most influential parameters. A larger λ' makes the update of $\sigma^2_{\mathrm{eff},l}$ more responsive but may weaken the damping effect, while a smaller λ' leads to smoother but slower convergence. The penalty factor ρ controls the strength of rank-one promotion. A too-small ρ may slow rank-one recovery, whereas a too-large ρ may overemphasize the penalty term. The parameters ϱ and ι further adjust the recovery tolerance and penalty-update speed. Overall, the adopted setting provides a practical balance among convergence stability, rank-one recovery accuracy, and computational efficiency. Unless otherwise specified, the remaining simulation parameters are configured as summarized in Table 1.

Table 1 Simulation parameters

Parameter	Value
Number of service group satellites, K	5
Number of CUEs, M	10
Number of NUEs, L	4
Maximum transmit power budget, $P_k^{\max}$	100 mA^2
Required minimum achievable rate, $R_m^{\min}$	3 bit/(s·Hz)
Speed of light, c	3×10^8 m/s
Signal frequency, f	35 GHz
Rain attenuation mean, μ_{r}	−2.6 dB
Rain attenuation variance, σ_{r}^2	1.63 dB

First, we investigate the convergence behavior of the proposed algorithm for different numbers of cooperative satellites in the service group. In Fig. 3, the vertical axis represents the objective function of the proposed algorithm, namely, $\frac{1}{L}\sum_{l=1}^{L} \mathrm{tr}\,(\mathbf{CRB})$, which is simply referred to as the average CRB. It can be observed that the objective value decreases monotonically and very rapidly during the first several iterations, and the curves become nearly flat after 8–10 iterations, which confirms the fast convergence of the algorithm. Moreover, a larger number of cooperative satellites lead to a higher initial value because more satellites generate stronger mutual interference, resulting in a less favorable starting point. After convergence, the average CRB is significantly reduced as K increases. In particular, the case with $K = 9$ satellites attains the lowest average CRB, followed by the cases with $K = 7$ and $K = 5$, demonstrating that involving more cooperative satellites provides additional spatial diversity and design degrees of freedom, thus improving the positioning accuracy of the proposed CAPA-assisted ICAN system.

For performance comparison, we consider the following four benchmark schemes: (1) DPA scheme, where each CAPA is replaced by a conventional phased array with the same physical aperture and half-wavelength element spacing, and the per-element transmit weights are optimized under the same power and rate constraints (Zhang ZJ and Dai, 2023). (2) Navigation-centric scheme, which designs the transmit beamformers by minimizing the average CRB subject only to the transmit power constraint (31c) while ignoring the communication rate constraint (31b). The navigation-centric scheme is used only as a navigation-only reference rather than a feasible ICAN baseline. It helps quantify the CRB loss induced by enforcing communication QoS constraints. (3) Fourier-based scheme, where the continuous transmit beamformers on each CAPA are represented by Fourier series expansions and the corresponding coefficients are optimized under the same objective and constraints as the proposed algorithm (Zhang Y et al., 2025). (4) Zero forcing (ZF)-oriented scheme, where the transmit beamformers for communication signals are designed to satisfy ZF conditions at all CUEs, thereby canceling both inter-CUE interference and navigation interference, and the navigation component is subsequently designed under the remaining power budget (Zhao BQ et al., 2024).

Fig. 4 illustrates the average CRB versus the maximum transmit power budget $P_k^{\max}$ for the proposed algorithm and the four benchmark schemes. As expected, the average CRB of all schemes decreases monotonically with increasing $P_k^{\max}$, since a larger power budget improves the received SNR at the NUE. The navigation-centric scheme attains the lowest

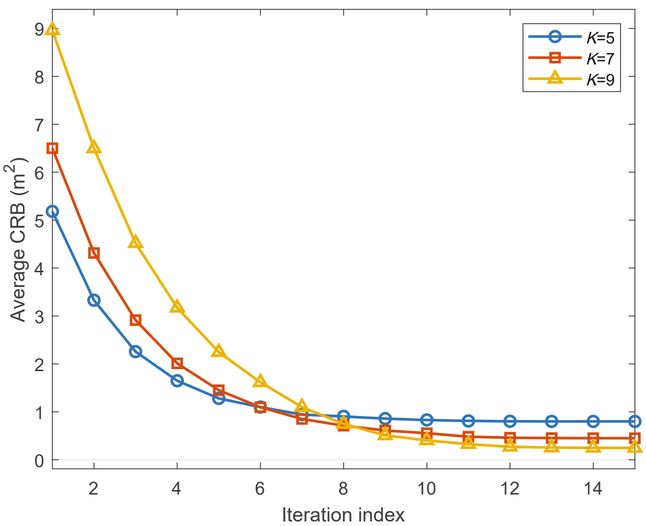

Fig. 3 Convergence behavior of the proposed algorithm

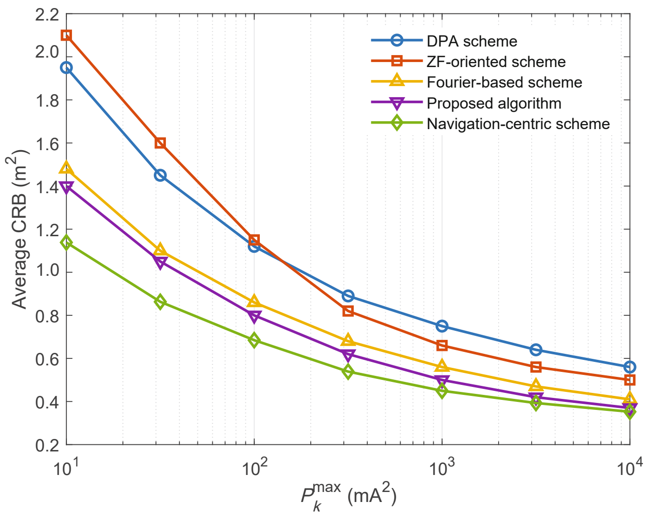

Fig. 4 Average CRB versus the maximum transmit power budget

CRB across the whole range, since it is optimized solely for navigation accuracy. The proposed algorithm closely follows this lower bound, especially in the medium-to-high power regime, demonstrating an effective balance between communication QoS and navigation accuracy. The Fourier-based scheme achieves a performance close to the proposed algorithm, but its reliance on high-order Fourier series expansions leads to much higher computational complexity, making it less appealing in practice. In contrast, the DPA and ZF-oriented schemes exhibit noticeable performance loss. The DPA scheme is limited by the reduced spatial degrees of freedom of discrete arrays, while the ZF-oriented scheme has the highest average CRB in the low-power regime because of the stringent zero-forcing constraints. As $P_k^{\max}$ increases, the ZF-oriented scheme benefits from the larger power budget and its performance becomes closer to that of the DPA and Fourier-based schemes.

Then, Fig. 5 shows how the average CRB varies with the required minimum achievable rate $R_m^{\min}$, thereby providing a direct illustration of the communication–navigation tradeoff. The navigation-centric scheme remains flat with respect to $R_m^{\min}$, since it ignores the communication rate constraint and optimizes only the navigation objective. In contrast, all rate-constrained schemes exhibit an increasing CRB as $R_m^{\min}$ becomes larger. This is because a higher rate requirement forces more transmit power and spatial degrees of freedom to be allocated to communication links and interference suppression, thereby reducing the resources available for navigation-oriented beamforming. Therefore, the increase in CRB can be interpreted as the navigation accuracy cost paid for guaranteeing higher communication throughput. Among these schemes, the proposed algorithm shows the smallest growth rate, as it jointly tailors the CAPA-based signal design to accommodate both the achievable rate and CRB requirements. The DPA and ZF-oriented schemes experience the steepest increase in CRB, because the DPA scheme offers fewer effective spatial degrees of freedom and strict zero-forcing constraints further restrict the design space, making these two schemes particularly sensitive to high-rate requirements.

Fig. 6 illustrates the impact of the effective radiating area A_T of the CAPAs on the average CRB. As A_T increases from 0.1 to 0.6 m^2, all schemes exhibit a sharp CRB reduction for small apertures and then gradually flatter, because a larger physical aperture provides higher array gain, finer angular resolution, and more orthogonal multiuser channels. The navigation-centric scheme consistently achieves the lowest CRB, and the proposed algorithm closely tracks it. The ZF-oriented scheme yields the highest CRB across all values of A_T. As A_T increases, its CRB decreases more rapidly and the gap to the other schemes becomes smaller. This is because a larger aperture improves channel orthogonality and makes the zero-forcing constraints easier to satisfy. On the other hand, a larger effective radiating area requires more hardware overhead and structural support, which increases payload cost and implementation complexity. Therefore, the choice of A_T should balance positioning accuracy against practical CAPA hardware constraints, including payload size and weight, structural support, thermal management, calibration, and continuous current-control precision, rather than simply maximizing the aperture size (Liu YW et al., 2025).

Next, Fig. 7 shows the impact of the number of CUEs M and NUEs L. The average CRB increases monotonically and

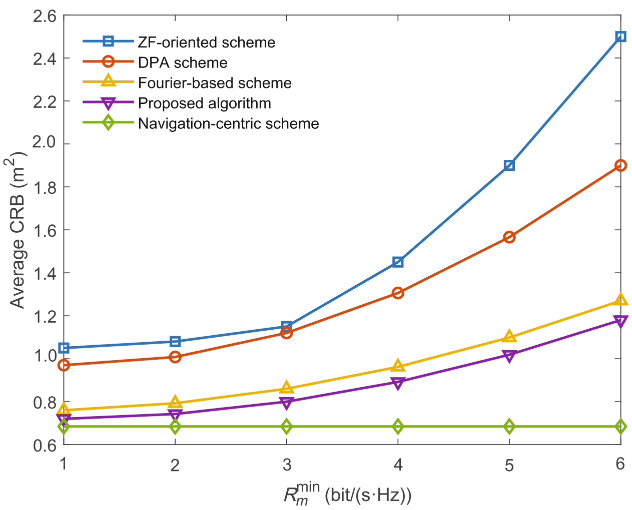

Fig. 5 Average CRB versus the required minimum achievable rate

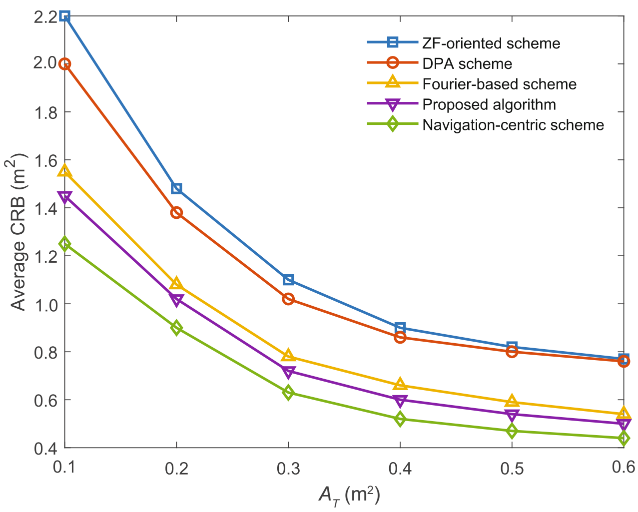

Fig. 6 Average CRB versus the effective radiating area of the CAPAs

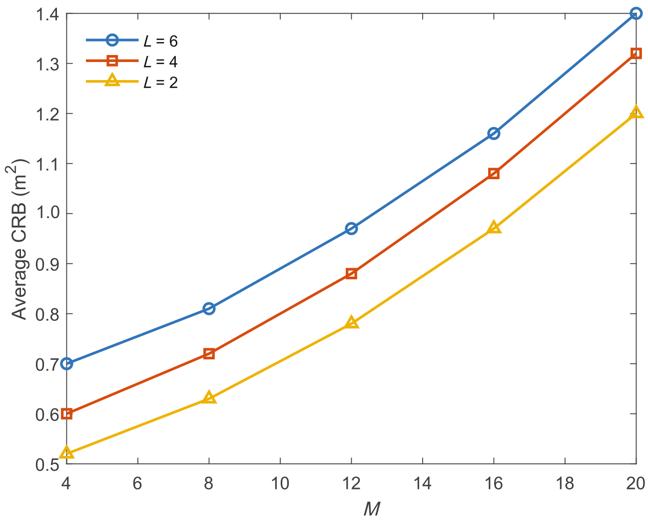

Fig. 7 Average CRB versus the number of CUEs for different numbers of NUEs

becomes steeper as M grows, because serving more CUE under the same CAPA aperture and power budget tightens the rate constraints and strengthens interference, so more power and spatial degrees of freedom must be allocated to communication rather than navigation. In addition, a larger number of NUEs lead to a higher average CRB, since the beamforming design must distribute navigation information over more spatial directions and the average is taken over a larger NUE set, including NUE with less favorable geometries. Therefore, this figure illustrates how network density gradually degrades positioning accuracy in the proposed CAPA-assisted ICAN system.

Last, Fig. 8 illustrates the impact of the orbital altitude h^* and the number of satellites per plane N^* on the average CRB. The average CRB drops quickly as N^* increases and then decreases more slowly, while lower orbital altitudes consistently yield better positioning performance. This is because a denser constellation improves geometry and cooperative gain with diminishing marginal returns, and closer satellites provide stronger signals and a wider angular spread. Overall, Fig. 8 indicates that constellation design plays a crucial role and that the satellite altitude and density should be selected by jointly considering positioning performance, atmospheric drag, satellite lifetime, frequent beam and handover management caused by fast LEO motion, inter-satellite coordination overhead, and launch and operation cost.

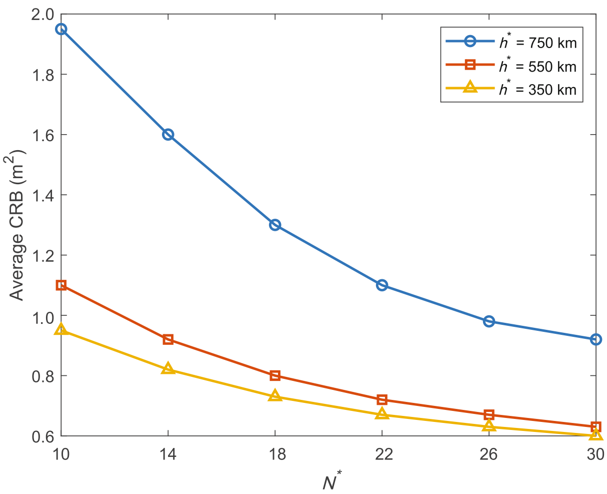

Fig. 8 Average CRB versus the number of satellites per plane for different orbital altitudes

5 Conclusions

This paper proposes an ICAN framework based on LEO satellite constellations, where an electromagnetic model is established for a dual-function LEO satellite equipped with CAPA. By introducing an ICAN channel subspace, the infinite-dimensional CAPA beamforming design is transformed into a finite-dimensional optimization problem that balances the achievable rate and CRB. Numerical results show that the proposed CAPA beamformer design algorithm yields notable ICAN performance gains over conventional DPA and other benchmark schemes, indicating the potential of CAPAs for future LEO satellite ICAN systems.

Acknowledgments

This work was supported by the Zhejiang Provincial Natural Science Foundation (Nos. LZ26F010002 and LQN25F010014) and the National Natural Science Foundation of China (Nos. U21A20443 and 62501222).

Author contributions

Qi WANG designed the research and processed the data. Qi WANG and Xiaoming CHEN drafted the paper. Qiao QI helped organize the paper. Zhaolin WANG and Yuanwei LIU revised and finalized the paper.

Conflict of interest

Xiaoming CHEN is a Junior Editorial Board Member of *ENGINEERING Information Technology & Electronic Engineering*, and he was not involved with the peer review process of this paper. All the authors declare that they have no conflict of interest.

Data availability

The data that support the findings of this study are available from the corresponding author upon reasonable request.

Declaration on the use of generative AI tools

During the preparation of this work, the authors used DeepSeek to improve language. After using this tool, the authors reviewed and edited the content as needed and take full responsibility for the content of the published article.

References

Al-Hourani A, 2021. Session duration between handovers in dense LEO satellite networks. *IEEE Wirel Commun Lett*, 10(12):2810-2814. https://doi.org/10.1109/LWC.2021.3118214

An J, Yuen C, Huang C, et al., 2023. A tutorial on holographic MIMO communications—Part II: performance analysis and holographic beamforming. *IEEE Commun Lett*, 27(7):1669-1673. https://doi.org/10.1109/LCOMM.2023.3278682

Closas P, Fernandez-Prades C, Fernandez-Rubio JA, 2007. Maximum likelihood estimation of position in GNSS. *IEEE Signal Process Lett*, 14(5):359-362. https://doi.org/10.1109/LSP.2006.888360

Closas P, Fernandez-Prades C, Fernandez-Rubio JA, 2009. Cramér–Rao bound analysis of positioning approaches in GNSS receivers. *IEEE Trans Signal Process*, 57(10):3775-3786. https://doi.org/10.1109/TSP.2009.2025083

Dardari D, 2020. Communicating with large intelligent surfaces: fundamental limits and models. *IEEE J Sel Areas Commun*, 38(11):2526-2537. https://doi.org/10.1109/JSAC.2020.3007036

Feng BK, Jenn DC, 2015. Two-way pattern grating lobe control for distributed digital subarray antennas. *IEEE Trans Antenn Propag*, 63(10):4375-4383. https://doi.org/10.1109/TAP.2015.2465863

Iannucci PA, Humphreys TE, 2024. Fused low-Earth-orbit GNSS. *IEEE Trans Aerosp Electron Syst*, 60(4):3730-3749. https://doi.org/10.1109/TAES.2022.3180000

Jensen MA, Wallace JW, 2008. Capacity of the continuous-space electromagnetic channel. *IEEE Trans Antenn Propag*, 56(2):524-531. https://doi.org/10.1109/TAP.2007.915416

Jin L, Wang LT, Jin XH, et al., 2022. Research on the application of LEO satellite in IoT. Proc 2nd IEEE Int Conf on Electronic Technology, Communication and Information, p.739-741. https://doi.org/10.1109/ICETCI55101.2022.9832117

Jin L, Xu XD, Han SJ, et al., 2024. Achievable rate of linear holographic MIMO with arbitrary aperture-length. *IEEE Trans Wirel Commun*, 23(11):16742-16756. https://doi.org/10.1109/TWC.2024.3446459

Li KX, You L, Wang JH, et al., 2022. Downlink transmit design for massive MIMO LEO satellite communications. *IEEE Trans Commun*, 70(2):1014-1028. https://doi.org/10.1109/TCOMM.2021.3131573

Lin SN, An JC, Gan L, et al., 2024. Stacked intelligent metasurface enabled LEO satellite communications relying on statistical CSI. *IEEE Wirel Commun Lett*, 13(5):1295-1299. https://doi.org/10.1109/LWC.2024.3368238

Liu JY, Chen ZY, Wang SX, et al., 2025. A joint time-frequency channel estimation method for ICAN-enabled LEO satellites. *IEEE Trans Veh Technol*, 74(11):18140-18145. https://doi.org/10.1109/TVT.2025.3574438

Liu YW, Ouyang CJ, Wang ZL, et al., 2025. CAPA: continuous-aperture arrays for revolutionizing 6G wireless communications. *IEEE Wirel Commun*, 32(4):38-45. https://doi.org/10.1109/MWC.001.2400493

Olver FW, Lozier DW, Boisvert RF, et al., 2010. NIST Handbook of Mathematical Functions. Cambridge University Press, Cambridge, UK.

Ouyang CJ, Liu YW, Zhang XQ, 2024. On the performance of continuous aperture array (CAPA)-based wireless communications. Proc IEEE Global Communications Conf, p.193-198. https://doi.org/10.1109/GLOBECOM52923.2024.10901526

Sanguinetti L, D'Amico AA, Debbah M, 2023. Wavenumber-division multiplexing in line-of-sight holographic MIMO communications. *IEEE Trans Wirel Commun*, 22(4):2186-2201. https://doi.org/10.1109/TWC.2022.3208961

Wang HQ, Shlezinger N, Eldar YC, et al., 2021. Dynamic metasurface antennas for MIMO-OFDM receivers with bit-limited ADCs. *IEEE Trans Commun*, 69(4):2643-2659. https://doi.org/10.1109/TCOMM.2020.3040761

Wang KY, So AMC, Chang TH, et al., 2014. Outage constrained robust transmit optimization for multiuser MISO downlinks: tractable approximations by conic optimization. *IEEE Trans Signal Process*, 62(21):5690-5705. https://doi.org/10.1109/TSP.2014.2354312

Wang Z, Zhang JY, Yi WH, et al., 2025. Analytical framework for effective degrees of freedom in near-field XL-MIMO. *IEEE Trans Wirel Commun*, 24(4):3465-3482. https://doi.org/10.1109/TWC.2025.3531418

Wang ZL, Mu XD, Liu YW, 2023. Stars enabled integrated sensing and communications. *IEEE Trans Wirel Commun*, 22(10):6750-6765. https://doi.org/10.1109/TWC.2023.3245297

Wang ZL, Ouyang CJ, Liu YW, 2025a. Beamforming optimization for continuous aperture array (CAPA)-based communications. *IEEE Trans Wirel Commun*, 24(6):5099-5113. https://doi.org/10.1109/TWC.2025.3545770

Wang ZL, Ouyang CJ, Liu YW, 2025b. Optimal beamforming for multi-user continuous aperture array (CAPA) systems. *IEEE Trans Commun*, 73(10):9207-9221. https://doi.org/10.1109/TCOMM.2025.3554644

Wang ZL, Ouyang CJ, Liu YW, 2026. Beamforming design for continuous aperture array (CAPA)-based MIMO systems. *IEEE Trans Wirel Commun*, 25:2167-2182. https://doi.org/10.1109/TWC.2025.3595157

Ying M, Chen XM, Qi Q, et al., 2024. Deep learning-based joint channel prediction and multibeam precoding for LEO satellite Internet of Things. *IEEE Trans Wirel Commun*, 23(10):13946-13960. https://doi.org/10.1109/TWC.2024.3406952

Ying M, Chen XM, Qi Q, et al., 2026. QoS-driven satellite constellation design for LEO satellite Internet of Things. *IEEE Trans Wirel Commun*, 25:3610-3625. https://doi.org/10.1109/TWC.2025.3605220

You L, Qiang XY, Zhu YX, et al., 2024. Integrated communications and localization for massive MIMO LEO satellite systems. *IEEE Trans Wirel Commun*, 23(9):11061-11075. https://doi.org/10.1109/TWC.2024.3378305

Zhang Y, Ouyang CJ, Shan HG, et al., 2025. Exploiting continuous-aperture arrays in integrated sensing and communication systems. *IEEE Trans Wirel Commun*, 24(11):9539-9555. https://doi.org/10.1109/TWC.2025.3573872

Zhang Y, Shan HG, Ouyang CJ, et al., 2026. Continuous-aperture array for integrated sensing and communication: rate-CRB tradeoff. *IEEE Trans Wirel Commun*, 25:4215-4230. https://doi.org/10.1109/TWC.2025.3609401

Zhang ZJ, Dai LL, 2023. Pattern-division multiplexing for multi-user continuous-aperture MIMO. *IEEE J Sel Areas Commun*, 41(8):2350-2366. https://doi.org/10.1109/JSAC.2023.3288244

Zhao BQ, Ouyang CJ, Zhang XQ, et al., 2024. On the performance of physical layer security for continuous-aperture array (CAPA) systems. https://doi.org/10.48550/arXiv.2412.13748

Zhao BQ, Ouyang CJ, Zhang XQ, et al., 2026. Downlink and uplink ISAC in continuous-aperture array (CAPA) systems. *IEEE Trans Wirel Commun*, 25:3592-3609. https://doi.org/10.1109/TWC.2025.3605158

Zhao JJ, Song HW, Cai KQ, et al., 2025. Continuous aperture array (CAPA)-based secure wireless communications. *IEEE Trans Commun*, 73(12):15474-15488. https://doi.org/10.1109/TCOMM.2025.3604315

Zorich VA, Paniagua O, 2016. Mathematical Analysis II (2nd Ed.). Springer Berlin, Heidelberg, Germany. https://doi.org/10.1007/978-3-662-48993-2

Appendix A: Derivation of $\nabla_{\boldsymbol{q}_l} h_{k,l}^{\mathrm{N}}$ in Eq. (26)

Herein, we provide the explicit derivation of the gradient of the navigation channel response with respect to the NUE's position, i.e., $\nabla_{\boldsymbol{q}_l} h_{k,l}^{\mathrm{N}}(\boldsymbol{s}_k', \boldsymbol{q}_l)$. This quantity is required both by the DPE algorithm and by the CRB evaluation in the main text. From Eq. (10), the navigation channel response is given by $h_{k,l}^{\mathrm{N}}(\boldsymbol{s}_k', \boldsymbol{q}_l)$. By substituting Green's function expression in Eq. (8) into Eq. (10), the channel response can be factorized as

$$h_{k,l}^{\mathrm{N}}(\boldsymbol{s}_k', \boldsymbol{q}_l) = C_{k,l}\, f_{\mathrm{prop}}(\boldsymbol{q}_l)\, f_{\mathrm{proj}}(\boldsymbol{q}_l), \tag{A1}$$

where $C_{k,l} = -\mathrm{j}\eta\xi_{\mathrm{r}}^{1/2}\mathrm{e}^{-\mathrm{j}\psi_{k,l}}/(2\lambda)$ is a constant independent of $\boldsymbol{q}_l$. The propagation $f_{\mathrm{prop}}(\boldsymbol{q}_l)$ and projection $f_{\mathrm{proj}}(\boldsymbol{q}_l)$ terms are given by

$$f_{\mathrm{prop}}(\boldsymbol{q}_l) = \frac{\mathrm{e}^{-\mathrm{j}\frac{2\pi}{\lambda}d_{k,l}}}{d_{k,l}}, \tag{A2}$$

$$f_{\mathrm{proj}}(\boldsymbol{q}_l) = \boldsymbol{u}_l^{\mathrm{T}}\left(\boldsymbol{I}_3 - \frac{\boldsymbol{v}_{k,l}\boldsymbol{v}_{k,l}^{\mathrm{T}}}{d_{k,l}^2}\right)\hat{\boldsymbol{u}}_{k,y}, \tag{A3}$$

with the geometric vector $\boldsymbol{v}_{k,l} = \boldsymbol{q}_l - \boldsymbol{s}_k(\boldsymbol{s}_k')$ and its norm $d_{k,l} = \|\boldsymbol{v}_{k,l}\|$. Since $\boldsymbol{s}_k(\boldsymbol{s}_k')$ does not depend on $\boldsymbol{q}_l$, we have $\nabla_{\boldsymbol{q}_l}\boldsymbol{v}_{k,l} = \boldsymbol{I}_3$, and thus gradients with respect to $\boldsymbol{q}_l$ can be equivalently computed with respect to $\boldsymbol{v}_{k,l}$. By applying the product rule, the gradient of $h_{k,l}^{\mathrm{N}}$ is given by

$$\nabla_{\boldsymbol{q}_l} h_{k,l}^{\mathrm{N}} = C_{k,l}\left[(\nabla_{\boldsymbol{q}_l} f_{\mathrm{prop}}) f_{\mathrm{proj}} + f_{\mathrm{prop}}(\nabla_{\boldsymbol{q}_l} f_{\mathrm{proj}})\right]. \tag{A4}$$

First, we derive the gradient of the propagation term $\nabla_{\boldsymbol{q}_l} f_{\mathrm{prop}}$. The gradient of the distance $d_{k,l}$ can be expressed as

$$\nabla_{\boldsymbol{q}_l} d_{k,l} = \frac{\boldsymbol{v}_{k,l}}{d_{k,l}}. \tag{A5}$$

Using the chain rule, we obtain

$$\nabla_{\boldsymbol{q}_l} f_{\mathrm{prop}}(\boldsymbol{q}_l) = \left(-\mathrm{j}\frac{2\pi}{\lambda d_{k,l}} - \frac{1}{d_{k,l}^2}\right)\frac{\mathrm{e}^{-\mathrm{j}\frac{2\pi}{\lambda}d_{k,l}}}{d_{k,l}}\boldsymbol{v}_{k,l}. \tag{A6}$$

Next, we compute the gradient of the projection term $\nabla_{\boldsymbol{q}_l} f_{\mathrm{proj}}(\boldsymbol{q}_l)$. By expanding the quadratic form, $f_{\mathrm{proj}}(\boldsymbol{q}_l)$ can be rewritten as

$$f_{\mathrm{proj}}(\boldsymbol{q}_l) = (\boldsymbol{u}_l^{\mathrm{T}}\hat{\boldsymbol{u}}_{k,y}) - \frac{N}{D}, \tag{A7}$$

where $N = (\boldsymbol{u}_l^{\mathrm{T}}\boldsymbol{v}_{k,l})(\boldsymbol{v}_{k,l}^{\mathrm{T}}\hat{\boldsymbol{u}}_{k,y})$ and $D = d_{k,l}^2 = \boldsymbol{v}_{k,l}^{\mathrm{T}}\boldsymbol{v}_{k,l}$. The term $\boldsymbol{u}_l^{\mathrm{T}}\hat{\boldsymbol{u}}_{k,y}$ is constant with respect to $\boldsymbol{q}_l$. Since $\boldsymbol{v}_{k,l}$ is an affine function of $\boldsymbol{q}_l$ with a unit Jacobian, we can equivalently compute the gradient with respect to $\boldsymbol{v}_{k,l}$, i.e., $\nabla_{\boldsymbol{q}_l} = \nabla_{\boldsymbol{v}_{k,l}}$. The gradients of N and D with respect to $\boldsymbol{v}_{k,l}$ are given by

$$\nabla_{\boldsymbol{v}_{k,l}} N = \boldsymbol{u}_l(\boldsymbol{v}_{k,l}^{\mathrm{T}}\hat{\boldsymbol{u}}_{k,y}) + \hat{\boldsymbol{u}}_{k,y}(\boldsymbol{u}_l^{\mathrm{T}}\boldsymbol{v}_{k,l}), \tag{A8}$$

$$\nabla_{\boldsymbol{v}_{k,l}} D = 2\boldsymbol{v}_{k,l}. \tag{A9}$$

$$\begin{aligned}\nabla_{\boldsymbol{q}_l} h^{\mathrm{N}}_{k,l}(\boldsymbol{s}'_k,\boldsymbol{q}_l) =& C_{k,l}\Bigg[\underbrace{\left(\left(-\mathrm{j}\frac{2\pi}{\lambda d_{k,l}^2}-\frac{1}{d_{k,l}^3}\right)\mathrm{e}^{-\mathrm{j}\frac{2\pi}{\lambda}d_{k,l}}\boldsymbol{v}_{k,l}\right)}_{\nabla f_{\mathrm{prop}}}\cdot\underbrace{\left(\boldsymbol{u}_l^{\mathrm{T}}\left(\boldsymbol{I}_3-\frac{\boldsymbol{v}_{k,l}\boldsymbol{v}_{k,l}^{\mathrm{T}}}{d_{k,l}^2}\right)\hat{\boldsymbol{u}}_{k,y}\right)}_{f_{\mathrm{proj}}}\\ &+\underbrace{\left(\frac{\mathrm{e}^{-\mathrm{j}\frac{2\pi}{\lambda}d_{k,l}}}{d_{k,l}}\right)}_{f_{\mathrm{prop}}}\cdot\underbrace{\left(\frac{2(\boldsymbol{u}_l^{\mathrm{T}}\boldsymbol{v}_{k,l})(\boldsymbol{v}_{k,l}^{\mathrm{T}}\hat{\boldsymbol{u}}_{k,y})\boldsymbol{v}_{k,l}-d_{k,l}^2\left[\boldsymbol{u}_l(\boldsymbol{v}_{k,l}^{\mathrm{T}}\hat{\boldsymbol{u}}_{k,y})+\hat{\boldsymbol{u}}_{k,y}(\boldsymbol{u}_l^{\mathrm{T}}\boldsymbol{v}_{k,l})\right]}{d_{k,l}^4}\right)}_{\nabla f_{\mathrm{proj}}}\Bigg].\end{aligned} \tag{A11}$$

Applying the quotient rule to $-N/D$, we have

$$\begin{aligned}\nabla_{\boldsymbol{q}_l} f_{\mathrm{proj}}(\boldsymbol{q}_l) &= -\frac{(\nabla_{\boldsymbol{v}_{k,l}}N)D-N(\nabla_{\boldsymbol{v}_{k,l}}D)}{D^2}\\ &=-\frac{1}{d_{k,l}^4}\Big(d_{k,l}^2\left[\boldsymbol{u}_l(\boldsymbol{v}_{k,l}^{\mathrm{T}}\hat{\boldsymbol{u}}_{k,y})+\hat{\boldsymbol{u}}_{k,y}(\boldsymbol{u}_l^{\mathrm{T}}\boldsymbol{v}_{k,l})\right]\\ &\quad -2(\boldsymbol{u}_l^{\mathrm{T}}\boldsymbol{v}_{k,l})(\boldsymbol{v}_{k,l}^{\mathrm{T}}\hat{\boldsymbol{u}}_{k,y})\boldsymbol{v}_{k,l}\Big).\end{aligned} \tag{A10}$$

Finally, substituting the expressions of $\nabla_{\boldsymbol{q}_l} f_{\mathrm{prop}}$ and $\nabla_{\boldsymbol{q}_l} f_{\mathrm{proj}}$ into Eq. (A4) yields the closed-form gradient of the navigation channel response, which is expressed as Eq. (A11) at the top of this page.

Appendix B: Proof of Theorem 1

Let $\mathcal{C}_k$ denote the finite-dimensional ICAN channel subspace in Eq. (32) and $\mathcal{C}_k^{\perp}$ be its orthogonal complement over $\boldsymbol{S}'_k$ under the inner product:

$$\int_{\boldsymbol{S}'_k} f_k^*(\boldsymbol{s}'_k)\, g_k(\boldsymbol{s}'_k)\,\mathrm{d}\boldsymbol{s}'_k=0,\quad f_k\in\mathcal{C}_k,\ g_k\in\mathcal{C}_k^{\perp}. \tag{B1}$$

Consider an arbitrary optimal solution $\{w_{k,m}(\boldsymbol{s}'_k), v_k(\boldsymbol{s}'_k)\}$ to problem (31). For each $w_{k,m}(\boldsymbol{s}'_k)$, take its orthogonal decomposition with respect to $\mathcal{C}_k$ and $\mathcal{C}_k^{\perp}$ as

$$w_{k,m}(\boldsymbol{s}'_k)=w_{k,m}^{\parallel}(\boldsymbol{s}'_k)+w_{k,m}^{\perp}(\boldsymbol{s}'_k), \tag{B2}$$

where $w_{k,m}^{\parallel}(\boldsymbol{s}'_k)\in\mathcal{C}_k$ and $w_{k,m}^{\perp}(\boldsymbol{s}'_k)\in\mathcal{C}_k^{\perp}$. Similarly,

$$v_k(\boldsymbol{s}'_k)=v_k^{\parallel}(\boldsymbol{s}'_k)+v_k^{\perp}(\boldsymbol{s}'_k), \tag{B3}$$

with $v_k^{\parallel}(\boldsymbol{s}'_k)\in\mathcal{C}_k$ and $v_k^{\perp}(\boldsymbol{s}'_k)\in\mathcal{C}_k^{\perp}$. For notational simplicity, the dependence on s'_k will be omitted in the following, and we write $w_{k,m}$, v_k, $w_{k,m}^{\parallel}$, $w_{k,m}^{\perp}$, $v_k^{\parallel}$, and $v_k^{\perp}$ instead.

First, we show that the orthogonal components $w_{k,m}^{\perp}$ and $v_k^{\perp}$ do not affect any performance-relevant quantity. From the received signal expressions in Eqs. (11), (16), and (20) and the effective noise variance in Eq. (22), every term in the communication achievable rate R_m, the navigation mean vectors $\boldsymbol{\mu}_l$, and the CRB matrix can be written as a linear function in the form $\int_{\boldsymbol{S}'_k} h^{\mathrm{C}}_{k,m}(\boldsymbol{s}'_k,\boldsymbol{p}_m)\, w_{k,i}\,\mathrm{d}\boldsymbol{s}'_k$ or $\int_{\boldsymbol{S}'_k} h^{\mathrm{N}}_{k,l}(\boldsymbol{s}'_k,\boldsymbol{q}_l)\, v_k\,\mathrm{d}\boldsymbol{s}'_k$. By the definition of $\mathcal{C}_k$, the conjugate kernels $h^{\mathrm{C}}_{k,m}(\cdot,\boldsymbol{p}_m)^*$ and $h^{\mathrm{N}}_{k,l}(\cdot,\boldsymbol{q}_l)^*$ belong to $\mathcal{C}_k$. Together with Eq. (B1), we have

$$\int_{\boldsymbol{S}'_k} h^{\mathrm{C}}_{k,m}(\boldsymbol{s}'_k,\boldsymbol{p}_m)\, w_{k,i}^{\perp}\,\mathrm{d}\boldsymbol{s}'_k=0, \tag{B4}$$

$$\int_{\boldsymbol{S}'_k} h^{\mathrm{N}}_{k,l}(\boldsymbol{s}'_k,\boldsymbol{q}_l)\, v_k^{\perp}\,\mathrm{d}\boldsymbol{s}'_k=0. \tag{B5}$$

Hence, all linear functions depend only on $w_{k,m}^{\parallel}$ and $v_k^{\parallel}$. As a result, replacing each $w_{k,m}$ by $w_{k,m}^{\parallel}$ and each v_k by $v_k^{\parallel}$ leaves R_m, $\boldsymbol{\mu}_l$, and **CRB** unchanged.

Next, we examine the transmit power. According to Eq. (5) and the orthogonal decompositions, we have

$$\int_{\boldsymbol{S}'_k}|w_{k,m}|^2\,\mathrm{d}\boldsymbol{s}'_k=\int_{\boldsymbol{S}'_k}\left(|w_{k,m}^{\parallel}|^2+|w_{k,m}^{\perp}|^2\right)\mathrm{d}\boldsymbol{s}'_k, \tag{B6}$$

$$\int_{\boldsymbol{S}'_k}|v_k|^2\,\mathrm{d}\boldsymbol{s}'_k=\int_{\boldsymbol{S}'_k}\left(|v_k^{\parallel}|^2+|v_k^{\perp}|^2\right)\mathrm{d}\boldsymbol{s}'_k. \tag{B7}$$

Therefore, discarding $w_{k,m}^{\perp}$ and $v_k^{\perp}$ does not increase the transmit power, while preserving feasibility and the objective value of problem (31).

Finally, let $\tilde{w}_{k,m}=w_{k,m}^{\parallel}$ and $\tilde{v}_k=v_k^{\parallel}$. Then $\{\tilde{w}_{k,m},\tilde{v}_k\}$ are feasible for problem (31), attain the same achievable rates and CRB as the original optimal solution, and satisfy $\tilde{w}_{k,m}(\boldsymbol{s}'_k),\tilde{v}_k(\boldsymbol{s}'_k)\in\mathcal{C}_k$. Therefore, an optimal solution with all beamformers lying in $\mathcal{C}_k$ always exists, which proves Theorem 1.

Appendix C: Derivation of the penalty-based SCA approximation

To handle the non-convex rank-one constraints in problem (54c), we employ a penalty-based method that incorporates these constraints into the objective function. This approach is part of an SCA framework, where the non-convex problem is iteratively approximated by a sequence of solvable convex problems. Specifically, for a nonzero positive semidefinite matrix $\boldsymbol{X}$, the condition $\mathrm{Rank}(\boldsymbol{X})=1$ is equivalent to

$$\mathrm{tr}(\boldsymbol{X})-\lambda_{\max}(\boldsymbol{X})=0, \tag{C1}$$

where $\lambda_{\max}(\cdot)$ denotes the maximum eigenvalue. Since $\mathrm{tr}(\boldsymbol{X})-\lambda_{\max}(\boldsymbol{X})$ is always non-negative for a positive semidefinite matrix, we can penalize any deviation from the rank-one structure by adding the term

$$\rho\left(\sum_{m=1}^{M}\left(\mathrm{tr}(\boldsymbol{A}_m)-\lambda_{\max}(\boldsymbol{A}_m)\right)+\left(\mathrm{tr}(\boldsymbol{B})-\lambda_{\max}(\boldsymbol{B})\right)\right) \tag{C2}$$

to the objective function, where $\rho>0$ is a penalty parameter. The resulting objective function becomes a difference-of-convex (DC) problem, since the maximum eigenvalue function $\lambda_{\max}(\cdot)$ is convex. It can be effectively handled by linearizing the concave component, i.e., $-\lambda_{\max}(\cdot)$, at each iteration. At the t^{th} iteration, we replace $\lambda_{\max}(\boldsymbol{A}_m)$ with its first-order Taylor expansion around the solution from the previous iteration $\boldsymbol{A}_m^{(t-1)}$, which is given by

$$\lambda_{\max}(\boldsymbol{A}_m^{(t-1)}) + \operatorname{tr}\left(\left(\boldsymbol{u}_{\boldsymbol{A}_m}^{(t-1)}\left(\boldsymbol{u}_{\boldsymbol{A}_m}^{(t-1)}\right)^{\mathrm{H}}\right)\left(\boldsymbol{A}_m - \boldsymbol{A}_m^{(t-1)}\right)\right), \tag{C3}$$

where $\boldsymbol{u}_{\boldsymbol{A}_m}^{(t-1)}$ is the principal eigenvector of $\boldsymbol{A}_m^{(t-1)}$. Since constant terms do not affect the optimization, we can simplify the approximation of $\lambda_{\max}(\boldsymbol{A}_m)$ to $\left(\boldsymbol{u}_{\boldsymbol{A}_m}^{(t-1)}\right)^{\mathrm{H}}\boldsymbol{A}_m\boldsymbol{u}_{\boldsymbol{A}_m}^{(t-1)}$. Similarly, $\lambda_{\max}(\boldsymbol{B})$ is linearized around the solution from the previous iteration $\boldsymbol{B}^{(t-1)}$, and $\boldsymbol{u}_{\boldsymbol{B}}^{(t-1)}$ denotes the principal eigenvector of $\boldsymbol{B}^{(t-1)}$. Since the constant terms do not affect the optimization, the approximation of $\lambda_{\max}(\boldsymbol{B})$ is simplified to $\left(\boldsymbol{u}_{\boldsymbol{B}}^{(t-1)}\right)^{\mathrm{H}}\boldsymbol{B}\boldsymbol{u}_{\boldsymbol{B}}^{(t-1)}$. Substituting the above linearized approximations into the penalty term (C2) yields the penalty-based optimization objective function.